

A submillimetre survey of the kinematics of the Perseus molecular cloud: I. data

Emily I. Curtis^{1,2*}, John S. Richer^{1,2} and Jane V. Buckle^{1,2}

¹ *Astrophysics Group, Cavendish Laboratory, J. J. Thomson Avenue, Cambridge, CB3 0HE*

² *Kavli Institute for Cosmology, c/o Institute of Astronomy, University of Cambridge, Madingley Road, Cambridge, CB3 0HA*

Accepted 2009 September 2

ABSTRACT

We present submillimetre observations of the $J = 3 \rightarrow 2$ rotational transition of ^{12}CO , ^{13}CO and C^{18}O across over 600 arcmin^2 of the Perseus molecular cloud, undertaken with HARP, a new array spectrograph on the James Clerk Maxwell Telescope. The data encompass four regions of the cloud, containing the largest clusters of dust continuum condensations: NGC1333, IC348, L1448 and L1455. A new procedure to remove striping artefacts from the raw HARP data is introduced. We compare the maps to those of the dust continuum emission mapped with SCUBA (Hatchell et al. 2005) and the positions of starless and protostellar cores (Hatchell et al. 2007a). No straightforward correlation is found between the masses of each region derived from the HARP CO and SCUBA data, underlining the care that must be exercised when comparing masses of the same object derived from different tracers. From the $^{13}\text{CO}/\text{C}^{18}\text{O}$ line ratio the relative abundance of the two species ($[\text{C}^{18}\text{O}]/[\text{C}^{13}\text{O}] \sim 7$) and their opacities (typically τ is 0.02–0.22 and 0.15–1.52 for the C^{18}O and ^{13}CO gas respectively) are calculated. C^{18}O is optically thin nearly everywhere, increasing in opacity towards star-forming cores but not beyond $\tau_{18} \sim 0.9$. Assuming the ^{12}CO gas is optically thick we compute its excitation temperature, T_{ex} (around 8–30 K), which has little correlation with estimates of the dust temperature.

Key words: submillimetre – stars: formation – ISM: kinematics and dynamics – ISM: individual: Perseus.

1 INTRODUCTION

Recent advances in telescope instrumentation have provided an unprecedented view of the star formation process inside molecular clouds. Near-infrared imaging from e.g. *Spitzer* (e.g. Evans et al. 2009) captures the youngest stellar objects, whilst (sub)millimetre continuum imaging with e.g. SCUBA or MAMBO maps the very earliest stages of star formation, often before a well-defined central object is established (e.g. Motte, Andre & Neri 1998; Johnstone et al. 2000; Hatchell et al. 2005; Enoch et al. 2006; Di Francesco et al. 2008). Simulations of star formation have also become increasingly sophisticated (e.g. Klessen & Burkert 2000; Bate & Bonnell 2005; Bate 2009a) with the latest models including turbulence, magnetic fields and radiative transfer (Price & Bate 2008; Bate 2009b). The true, underlying structure in star-forming clouds, essential for comparison with models, is hard to disentangle from continuum images alone (Ballesteros-Paredes & Mac Low 2002; Smith, Clark & Bonnell 2008b): density enhancements along the line of sight may superpose and limited spatial resolution and sensitivity inevitably blends nearby objects together. Spectral lines from

molecular species can provide crucial information about the *kinematics* of and physical conditions inside molecular clouds. They may for instance allow the separation of multiple objects, moving at distinct velocities, along a line of sight (e.g. Kirk, Johnstone & Tafalla 2007). Additionally, line emission is arguably the best discriminator between different support mechanisms for star-forming cores, i.e. whether magnetic fields or turbulence dominate the required suppression of star formation in the bulk of clouds.

This paper presents a new survey of the kinematics of star formation in the Perseus molecular cloud. We observed four fields, totalling approximately 600 arcmin^2 in the $J = 3 \rightarrow 2$ rotational transition of ^{12}CO , ^{13}CO and C^{18}O using HARP (Heterodyne Array Receiver Programme), a new array spectrograph operating between 325 and 375 GHz on the James Clerk Maxwell Telescope (JCMT, see Smith et al. 2003, 2008a; Buckle et al. 2009). These data represent some of the largest and highest-quality maps of the higher- J transitions of CO and its isotopologues with good angular resolution ($< 20 \text{ arcsec}$). This paper is the first in a planned series which will examine the gas structure and core kinematics (Paper II), molecular outflows (Paper III) and the physical conditions in the cloud cores (Paper IV). This paper is organized as follows: the remainder of the introduction outlines the survey and its aims before

* E-mail: e.curtis@mrao.cam.ac.uk

Table 1. The transitions of CO and its isotopologues observed.

Molecule	ΔJ^a	ν_{trans}^b (GHz)	T_{trans}^c (K)	n_{crit}^d (cm^{-3})
CO	3 \rightarrow 2	345.796	33.2	2.54×10^4
^{13}CO	3 \rightarrow 2	330.558	31.7	2.22×10^4
C^{18}O	3 \rightarrow 2	329.331	31.6	2.19×10^4

^a Transition quantum numbers.^b Rest frequency.^c Height of the upper J level above ground.^d Estimated critical density, assuming a collision cross-section $\sigma = 10^{-16} \text{ cm}^2$ and velocity 1 km s^{-1} so $n_{\text{crit}} = A \times 10^{10} \text{ cm}^{-2}$. The Einstein A values were taken from the LAMDA database (Schöier et al. 2005).

Sections 2 and 3 detail the observations and data reduction procedure including an algorithm to calibrate variable sensitivities across the HARP array for molecular cloud data. Section 4 presents maps of the integrated intensity of all of the isotopologues while some initial results including the cloud opacity and excitation temperature, assuming local thermodynamic equilibrium (LTE) are presented in Section 5. We summarize this work in Section 6.

1.1 The survey

The transitions of CO and its common isotopologues in the 345 GHz atmospheric window trace denser and/or warmer regions than their lower J relatives – compare the temperature of 5 K and density of $n_{\text{crit}} \sim 700 \text{ cm}^{-3}$ required to collisionally excite the $^{12}\text{CO } J = 1 \rightarrow 0$ line at 115 GHz to Table 1. These conditions are similar to those inside star-forming SCUBA cores, allowing us to probe the motions of bulk gas in their vicinity at matched resolution to SCUBA 850 μm observations. This survey is closely linked to the JCMT Gould Belt Legacy Survey (GBS, Ward-Thompson et al. 2007). Our data will eventually be included in that analysis and we share similar science goals, namely:

- (i) Map any high-velocity outflowing gas in the $^{12}\text{CO } J = 3 \rightarrow 2$ line to investigate mass-loss and accretion in a large sample of sources. The presence of an outflow can differentiate between a protostellar or starless continuum core, establishing the source age.
- (ii) Establish the level of non-thermal support inside star-forming cores from the C^{18}O transition, which may also be used to evaluate the levels of CO depletion.
- (iii) Investigate the turbulent structure of the molecular gas.

Perseus (see Fig. 1) is an intermediate star-forming environment between low-mass, quiescent Taurus and high-mass, turbulent Orion (e.g. Ladd, Lada & Myers 1993). The complex consists of a series of dark clouds at approximately $3^{\text{h}}30^{\text{m}}, +31^{\circ}$ with an angular extent of about (1.5×5) deg, totalling $\sim 1.7 \times 10^4 M_{\odot}$ (Bachiller & Cernicharo 1986a). The cloud is associated with Per OB2, the second closest OB association to the Sun, with an age $< 15 \text{ Myr}$ (see Bally et al. 2008). The association has blown a 20 deg diameter shell of atomic hydrogen into the interstellar medium with the Perseus molecular cloud embedded in its western rim. The region is well-studied both as a whole and in individual sub-sections with a wealth of ancillary data available, particularly from the COMPLETE project¹ (Ridge et al. 2006b).

¹ the COordinated Molecular Probe Line Extinction Thermal Emission survey of star-forming regions, see <http://www.cfa.harvard.edu/COMPLETE>

Notably, large-area surveys of the dust continuum emission in Perseus have been completed with SCUBA at 850 μm (Hatchell et al. 2005; Kirk, Johnstone & Di Francesco 2006) and Bolocam at 1.1 mm (Enoch et al. 2006). The 3 deg² SCUBA survey (Hatchell et al. 2005) identified 92 submillimetre cores above their completeness limit of $0.4 M_{\odot}$ (in a 14 arcsec beam). 80 per cent of these cores were grouped in six clusters: NGC1333, IC348, L1448, L1455, B1 and B5. The larger and more sensitive Bolocam survey (7.5 deg^2 down to $0.18 M_{\odot}$; Enoch et al. 2006) identified 122 compact cores. However, only 5–10 cores were in areas not observed with SCUBA by Hatchell et al., illustrating that most of Perseus is devoid of active star formation. In this survey we target the clusters of star-forming cores (see Section 2). *Spitzer* has provided a census of deeply embedded young stellar objects (YSOs) in many nearby molecular clouds (e.g. Evans et al. 2009) and this population has been associated with continuum cores identified by SCUBA (Jørgensen et al. 2007a, 2008) or Bolocam (Enoch et al. 2008, 2009). In this survey, we use the catalogue of Hatchell et al. (2007a), who identified the SCUBA cores from Hatchell et al. (2005) as starless, Class 0 or Class I protostars on the basis of their spectral energy distributions (SEDs), which incorporated *Spitzer* fluxes from the IRAC wavebands.²

Estimates of the distance to Perseus vary from 220 pc (Černis 1990) to 350 pc (Herbig & Jones 1983). Larger distances are often based on the Perseus OB2 association which has an established distance of $\sim 320 \text{ pc}$ from *Hipparcos* (de Zeeuw et al. 1999). However, there is some evidence that Per OB2 may lie behind the molecular clouds of interest which are probably at closer to 250 pc (Černis 1993). In fact, it may not be appropriate to use a single distance for the entire cloud and extinction studies suggest increasing distances from 220 to 260 pc from west to east (previous references and Černis & Straizys 2003). Furthermore many authors have suggested that Perseus is a superposition of a least two smaller clouds – the closer is thought to be an extension of Taurus with the more distant a shell-like structure (e.g. Ridge et al. 2006a). The latest and possibly most reliable measure of the distance to the H_2O maser in NGC1333 SVS13 found $(235 \pm 18) \text{ pc}$ using its parallax at radio frequencies (Hirota et al. 2008). In this survey we assume Perseus to be a single entity at a distance of 250 pc for consistency with the majority of recent studies e.g. the *Spitzer* Cores to Disks team, c2d (Evans et al. 2003, 2009) and the Bolocam Perseus survey (Enoch et al. 2006).

2 OBSERVATIONS

We selected the four largest clusters of continuum cores – NGC1333, IC348, L1448 and L1455 – to map in the ^{12}CO , ^{13}CO and $\text{C}^{18}\text{O } J = 3 \rightarrow 2$ lines (see Fig. 1; the exact areas are detailed in Table 2). All the regions were observed in the three tracers except for NGC1333 where only ^{13}CO and C^{18}O data were taken since it had already been observed in $^{12}\text{CO } J = 3 \rightarrow 2$ with HARP (J. Swift, personal communication).

The data were taken as part of the Guaranteed Time programme for the HARP instrument team, over a period of nine nights between 17th December 2007 and 12th January 2008 with one map of NGC1333 taken on 28th July 2007. The data comprise $\sim 43 \text{ hrs}$ total observing time, approximately 25 hrs on sky translating to an

² IRAC (Infrared Array Camera) on *Spitzer* has four channels at 3.6, 4.5, 5.8, and 8 μm .

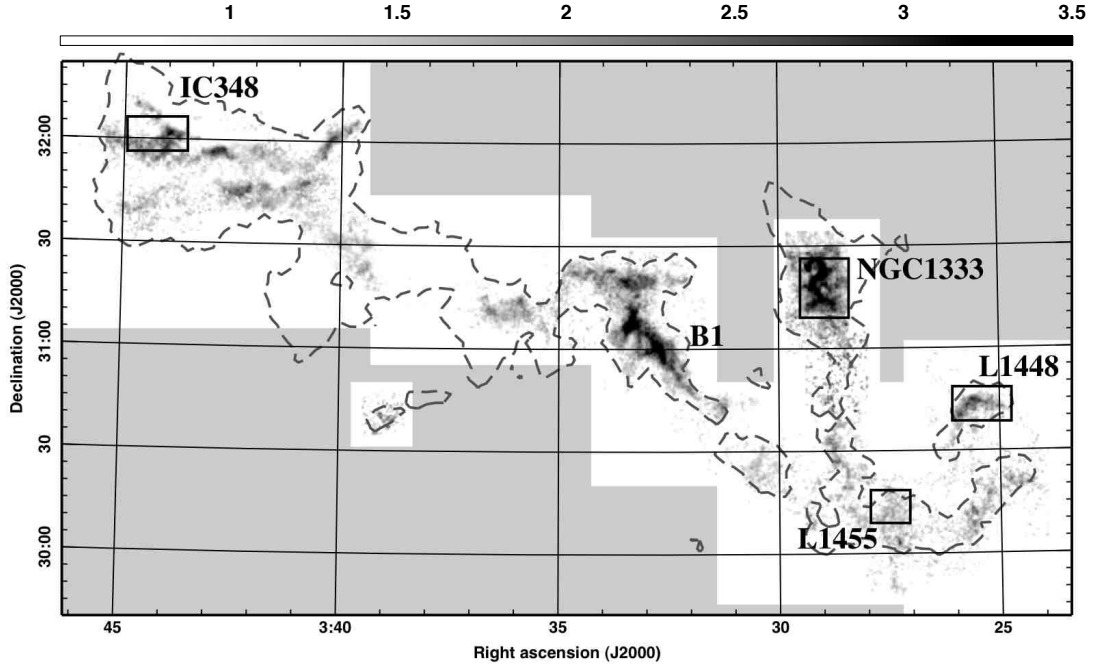


Figure 1. Overview of the molecular gas in the Perseus molecular cloud. The grey-scale is $C^{18}O J = 1 \rightarrow 0$ integrated intensity in $K km s^{-1}$ from the FCRAO 14-m telescope (Hatchell et al. 2005). The dotted contour encloses regions where the visual extinction is > 3.5 , from the map of the COMPLETE team (Ridge et al. 2006b). The four fields observed in this survey are enclosed in boxes: NGC1333, IC348, L1448 and L1455. Also marked is the B1 molecular ridge. B5 the other large cluster of SCUBA cores lies roughly 45 arcmin to the northeast.

Table 2. The regions observed.

Region	Centre ^a		Dimensions		Area (arcmin ²)
	RA (h m s)	Dec ($^{\circ}$ $'$ $''$)	Width (arcsec)	Height (arcsec)	
NGC1333	03:28:56	+31:17:30	760	900	190
IC348	03:44:14	+31:49:49	1100	650	199
L1448	03:25:30	+30:43:45	800	500	111
L1455	03:27:27	+30:14:30	880	520	127

^a Position of the map centre in J2000 coordinates.

observing efficiency of 58 per cent. The weather conditions were good to excellent throughout with median receiver and system temperatures of $T_{rx} = 180 K$ and $T_{sys} = 325 K$ for ^{12}CO compared to $T_{rx} = 179 K$ and $T_{sys} = 415 K$ for $^{13}CO/C^{18}O$.

The HARP imaging array comprises 16 SIS detectors, arranged on a 4×4 grid, separated by 30 arcsec. This under-samples the focal plane with respect to the Nyquist criterion ($\lambda/2D$ is 6.0 and 6.2 arcsec at 345 and 330 GHz respectively), therefore standard HARP observing strategies take data points in between the nominal detector positions to produce a fully-sampled map (see Buckle et al. 2009). The observations for this survey were taken in the raster mode at the default sample spacing of 7.3 arcsec. The ^{13}CO and $C^{18}O$ observations were taken simultaneously, utilizing the capability of the new back-end correlator, ACSIS (Auto-Correlation Spectral Imaging System, Buckle et al. 2009), to split its bandpass into two separate sub-bands. Both sub-bands provide $\sim 250 MHz$ of bandwidth on the two lines with a channel spacing of 61 kHz corresponding to approximately $0.05 km s^{-1}$. The ^{12}CO observations were also taken using a sub-band mode, with both centred at the same frequency: (i) for high-velocity gas with a bandwidth of

$\sim 1 GHz$, broken into channels 977 kHz wide ($0.8 km s^{-1}$) and (ii) to trace the gas in detail with $\sim 250 MHz$ bandwidth at a channel spacing of 61 kHz ($0.05 km s^{-1}$).

2.1 Scan strategy

During raster or “on-the-fly” mapping, the telescope scans continuously along a set direction (usually parallel to the longest side of the map), dumping the data gathered at discrete intervals – as little as 100 ms apart with HARP/ACSIS. Once the telescope has scanned the length of the map, it steps perpendicular to the scan direction and begins a new row. The HARP array is angled at $\arctan(1/4) \sim 14$ deg with respect to the scan direction to produce a fully-sampled image on a 7.3 arcsec grid (Buckle et al. 2009).

The detectors in HARP have varying responses across the array. Additionally, in any one observation the data from a number of detectors can be unusable with poor baselines. These in combination can lead to maps with variable noise or entirely blank strips. Our observing strategy employed three factors to reduce these effects:

- (i) The perpendicular spacing between scan rows was set to be half the width of the tilted array. Thus, in any row, half of the detectors are going over previously observed positions and half are scanning new parts of the sky.
- (ii) The most effective way to ‘fill-in’ entirely missing rows is to ‘basket-weave’ i.e. re-observe the map with the scan direction perpendicular to the original.
- (iii) A small offset between map repeats, of one pixel’s length perpendicular to the scan direction, will cause the new spectra from one detector to coincide with those from a different one in the previous repeat.

Each area was observed at least four times, with one repeat offset

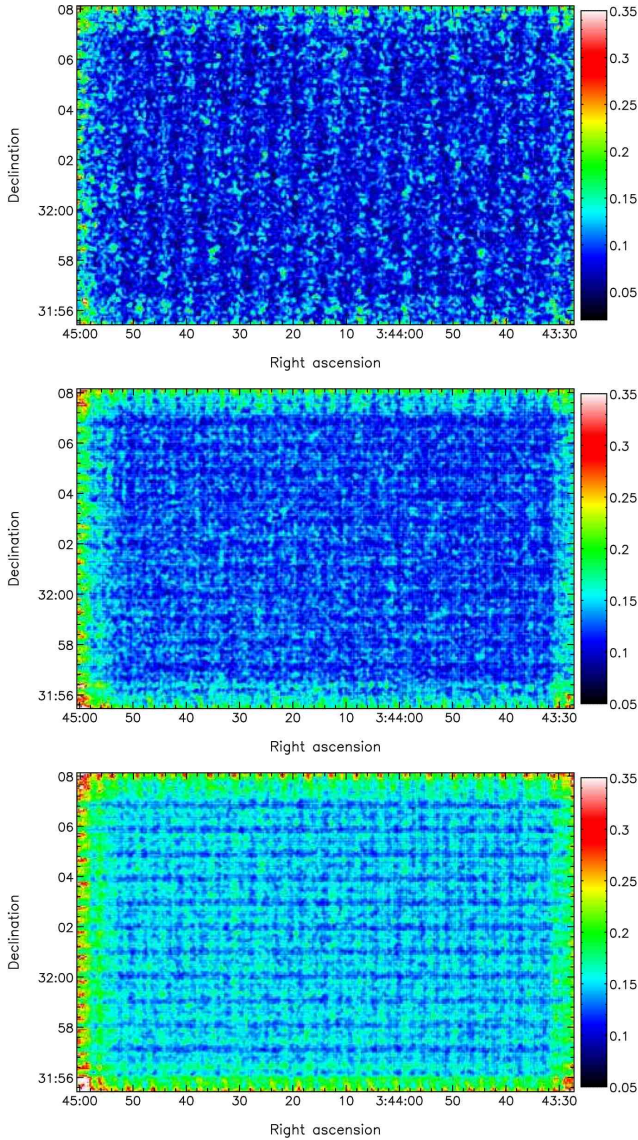


Figure 2. Representative maps of the RMS noise in K towards IC348 in the three CO isotopologues. Top: $^{12}\text{CO } J = 3 \rightarrow 2$ noise in 1 km s^{-1} channels. Middle and bottom: ^{13}CO and C^{18}O noise in 0.15 km s^{-1} channels respectively.

from the original and the other two basket-weaved variants of the original and offset scans. Maps of the resulting root mean square (RMS) noise for the three transitions towards IC348 are shown in Fig. 2.

2.2 References and calibrations

Finding reference positions has proved considerably harder for HARP than single-pixel receivers, as all 16 detectors must point at line-free regions, requiring a ‘blank’ piece of sky approximately 2 arcmin square. Three such positions were used for our Perseus survey (see Table 3). Separate one minute ‘stare’ observations were undertaken at $^{12}\text{CO } J = 3 \rightarrow 2$ towards these positions, using references even further from the cloud. All were found to have no emission above the noise, re-binned in 1 km s^{-1} velocity channels, in every working detector.

All the standard telescope observing procedures were fol-

Table 3. Reference positions used.

RA (J2000) (h m s)	Dec (J2000) ($^{\circ}$ $'$ $''$)	Sub-Region used
03:29:00	+31:52:30	NGC1333
03:48:38	+31:49:39	IC348
03:33:11	+31:52:02	L1448 and L1455

lowed. Calibration spectra were taken frequently towards CRL 618 of the ^{12}CO or $^{13}\text{CO } J = 3 \rightarrow 2$ lines as appropriate. The intensity in the reference detector was then compared to previously recorded standards and only if they matched within a calibration tolerance, were any subsequent observations allowed to continue. All the data products and images we present are on the antenna temperature scale (T_{A}^* , Kutner & Ulich 1981), which can be converted to main beam brightness temperature, T_{mb} , using $T_{\text{mb}} = T_{\text{A}}^*/\eta_{\text{mb}}$. The efficiency we use, $\eta_{\text{mb}} = 0.66$, was measured during the commissioning of HARP.

3 DATA REDUCTION

We used the Starlink software collection³ for the analysis and reduction of HARP data. First, bad or extremely noisy data were flagged in the supplied HARP time-series format. The resultant spectra were placed on to a spatial grid using the SMURF reduction package (Jenness et al. 2008). Our final data products are sampled on a 3 arcsec grid, using a 9 arcsec full-width half-maximum (FWHM) Gaussian gridding kernel, resulting in an equivalent FWHM beam size of 17.7 and 16.8 arcsec for $^{13}\text{CO}/\text{C}^{18}\text{O}$ and ^{12}CO respectively. After gridding, a linear baseline was removed from each spectrum by fitting line-free portions using the Starlink KAPPA applications. The spectra were also re-binned spectrally to resolutions of 0.15 km s^{-1} for $^{13}\text{CO}/\text{C}^{18}\text{O}$ and 1 km s^{-1} for the low-resolution ^{12}CO data.

3.1 The HARP flatfield

After the basic data reduction, distinctive stripes were apparent in the integrated intensity images. Near the peak of the line intensity, rows of high and low pixel values lay parallel to the scan direction, implying certain detectors were systematically higher or lower by as much as a factor of two. The worst affected data were from the ^{13}CO and high-resolution ^{12}CO scans (see Fig. 3). A similar pattern was clear in *every* individual scan.

The origin of such systematic calibration differences between detectors is unknown but is likely to be in the intermediate frequency system. However, for the purposes of this paper we require only a pragmatic method to eliminate the striping artefacts from molecular cloud data. Therefore, we derive a set of temperature conversion factors (TCFs), by which we can multiply the spectra from each detector to get them on to a common intensity scale. This procedure is similar to the ‘flatfield’ procedure which accounted for the flux conversion factors with SCUBA (Holland et al. 1999), therefore we refer to the analogous flatfield for HARP.

Ideally, to derive these factors from observations, one would

³ Now maintained and developed by the Joint Astronomy Centre, see <http://starlink.jach.hawaii.edu>

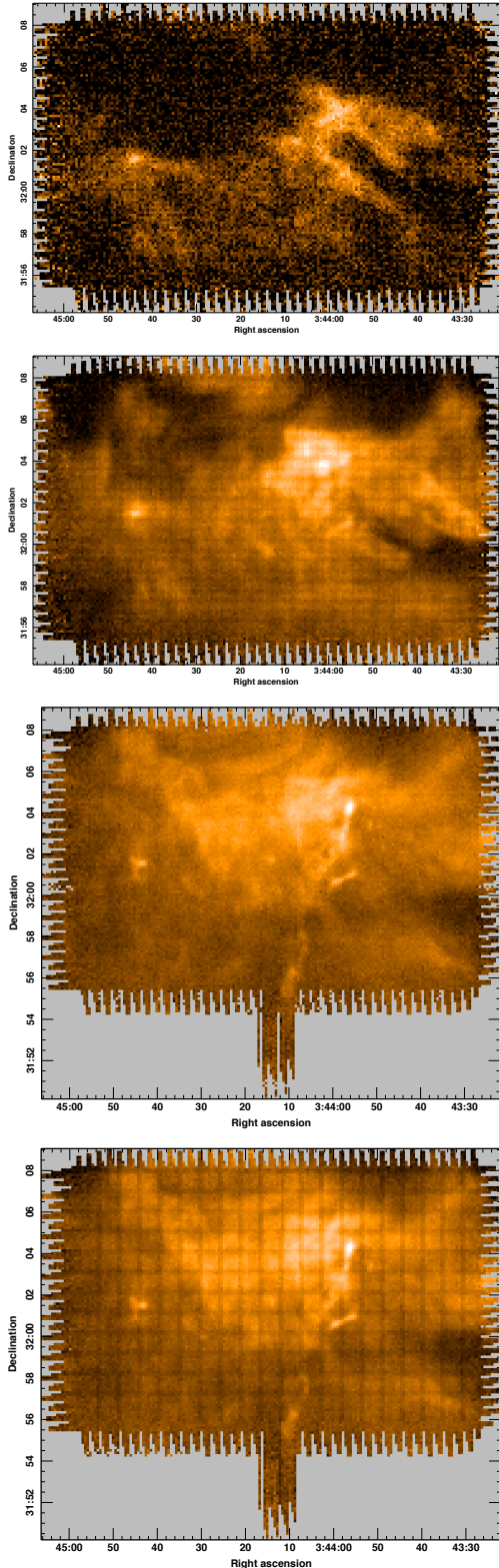


Figure 3. Integrated intensity images for the different $J = 3 \rightarrow 2$ transitions towards IC348 displaying the striping artefacts from our basic data reduction. The spectra are distributed on a 7.3 arcsec grid using nearest-neighbour allocation to emphasize detector based variations. From top to bottom are $C^{18}O$, ^{13}CO , ^{12}CO low-resolution and ^{12}CO high-resolution maps. The ^{12}CO data from a few telescope scan rows appear to have slipped, this is a known problem where the telescope does not return to the top of the map before commencing integrating.

observe a small source, providing a fully-sampled map for each detector, so that the total flux can be compared between them. However, we must derive the factors from the scientific observations themselves, comparing the intensity detector-by-detector for an entire map. First, datacubes were produced for each detector *individually* and the spectra integrated over the line and summed over the map. We divided the sum from the reference detector (R11, one of the central four in the array, see Buckle et al. 2009 for an explanation of how the JCMT points and tracks with HARP) by those from each of the other working detectors in turn (up to 15 in number), to calculate the respective TCF. The reference detector was taken as the intensity standard as it is not masked out in any of our observations. Additionally, all the calibrations are centred on it, so we have a robust determination of its performance. Once the factors are known, the output from each detector is multiplied by its respective TCF. The procedure worked very effectively for most of the data as shown in Fig. 4 and all the subsequent images in this paper have been multiplied by TCFs, except the $C^{18}O$ data towards L1455 which had an insufficient signal-to-noise ratio (SNR) and all the low-resolution ^{12}CO datasets, which did not display the artefacts.

It is perhaps surprising that this procedure worked so effectively and undoubtedly the nature of the targets contributed to its success. The method depends on each detector receiving exactly the same amount of emission. Offset map repeats and basket-weaving helped each detector to sample a larger proportion of the target field. However, it is the uniformity of a molecular cloud’s emission that means, in general, there is little difference in intensity between the different detectors. If there were many compact sources or intense emission towards the edges of these maps, which are only observed by a few detectors, then this technique would be ineffective. Other datasets taken in the same period show similar striping artefacts, notably those of the JCMT GBS, who have implemented our algorithm across a number of their fields.

4 RESULTS

4.1 NGC1333

NGC1333 is a young stellar cluster in the west of Perseus, associated with the reflection nebula of the same name and the dark cloud L1450. It has been widely studied (see Walawender et al. 2008 for a review) and is the most active region of star formation in the Perseus complex. The stellar cluster is very young (< 1 Myr) and highly obscured, containing about 150 stars totalling $79 M_{\odot}$ (Lada, Alves & Lada 1996; Wilking et al. 2004). The latest infrared (IR) survey with *Spitzer* (Jørgensen et al. 2006; Rebull et al. 2007; Gutermuth et al. 2008) identified 137 objects in the cluster: 98 pre-main sequence stars and 39 protostars. These protostars are correlated with the position of dense molecular material and dust. In total, there is approximately $450 M_{\odot}$ of gas in the region (Warin et al. 1996). Much of this gas lies in dense filaments, surrounding cavities (Lefloch et al. 1998; Quillen et al. 2005). The YSOs in NGC1333 also drive a large number of overlapping outflows, providing one of the clearest examples of the self-regulation of star formation (Knee & Sandell 2000).

We present maps of the ^{13}CO and $C^{18}O$ HARP data in Fig. 5, alongside the SCUBA $850 \mu m$ emission over the observed region, originally from observations by Sandell & Knee (2001) but later analysed as part of the survey of Hatchell et al. (2005). Qualitatively, the $C^{18}O$ and SCUBA maps closely resemble each other.

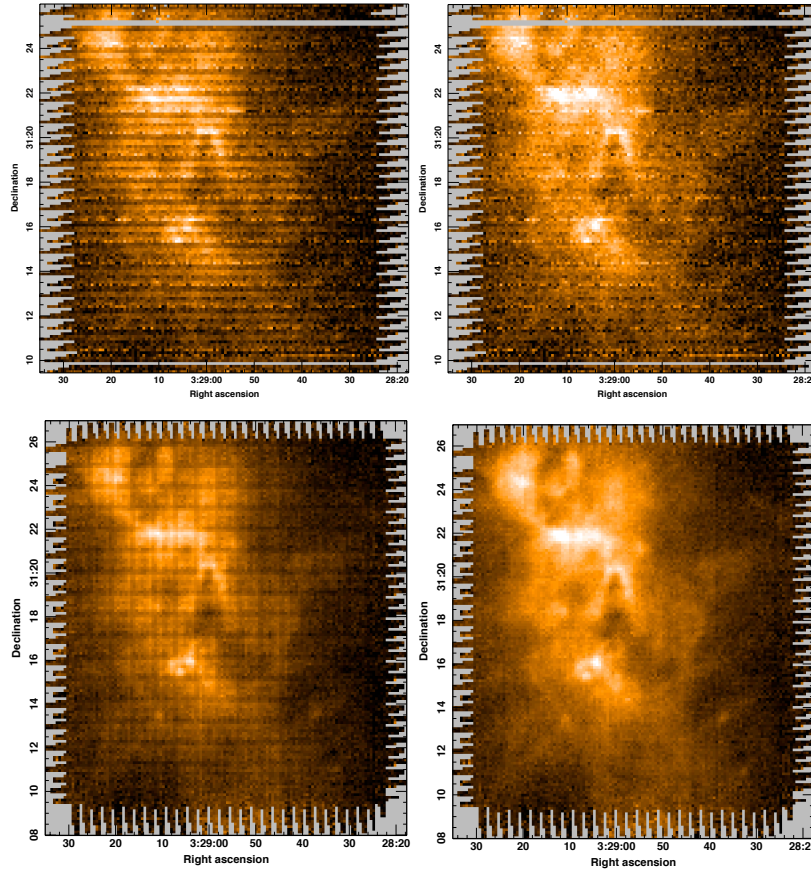


Figure 4. Action of the flatfield procedure on ^{13}CO integrated intensity images towards NGC1333. The panels are from top to bottom and left to right: data from a single scan, unaltered from the basic reduction; the same data as in the previous panel with the flatfield applied; data from all the NGC1333 scans, unaltered from the basic reduction; and the same data as in the previous panel but with the flatfield applied.

The central cavity, just north of SVS13 is clear in all the tracers, as is the horseshoe of emission enclosing its northern boundary. This would suggest that similar material is being explored in both the C^{18}O and SCUBA data. However, there are clear differences in the structures as well. IRAS4 and IRAS2 (Jennings et al. 1987), are two of the brightest sources in the SCUBA field, yet they have much weaker C^{18}O emission and can scarcely be discerned in the ^{13}CO data. The string of cores to the north of the central cavity, (sources 54, 56 and 66⁴) have quite weak SCUBA emission but are the brightest objects in the C^{18}O maps.

4.2 The IC348 molecular ridge

Our second field is in the vicinity of another young IR cluster (~ 2 Myr old), IC348 (see Herbst 2008 for a review), in the east of Perseus. It comprises several hundred members totalling about $160 M_{\odot}$ (Luhman et al. 2003). The low stellar disc fraction and lack of outflow activity may indicate that the cluster is coming to the end of its star-forming phase (Luhman et al. 1998). In fact the region we refer to as IC348 hereafter (Fig. 6) is really a bright molecular ridge some 10 arcmin southwest of the cluster, sometimes associated with the ‘‘Flying Ghost Nebula’’ (Boulard et al. 1995). This area, in contrast to IC348, is currently undergoing star formation

with many embedded objects and outflows, possibly triggered by the nearby cluster (e.g. Bally et al. 2008). The best-known feature in the area is HH211, a highly-collimated bipolar outflow driven by a Class 0 protostar discovered by McCaughrean, Rayner & Zinnecker (1994), which has been the target of many interferometric studies subsequently (e.g. Gueth & Guilloteau 1999; Chandler & Richer 2001).

In our C^{18}O data, depicted in Fig. 6, the close correspondence with the SCUBA emission is striking. Again there is not a simple scaling between SCUBA flux and C^{18}O integrated intensity, for example the brightest C^{18}O core is the starless source 17, while the driving source of HH211 (source 12), the brightest SCUBA core, is less prominent in C^{18}O . The ^{12}CO data looks very different, as it is probably optically thick (thus tracing only outer layers of the cloud) and has very bright outflow lobes. Two bipolar outflow structures can be seen in the ^{12}CO integrated intensity and are more obvious in the false colour red-green-blue (RGB) image of the same gas. The first highly symmetric outflow (driven by source 12) is HH211, while the second is the more confused north-south flow from source 13 – known also as IC348-MMS (Eisloffel et al. 2003) or IC348-SMM2 (Tafalla, Kumar & Bachiller 2006; Walawender et al. 2006). The bipolar outflow discovered by Tafalla et al. (2006) from IC348-SMM3 (source 15), slightly west of IC348-MMS, is also faintly discernible. Two Class I protostars (sources 14 and 101) are very red in the RGB image. This may indicate either an outflow where only one lobe is visible due to e.g. an inhomogeneous environment

⁴ The source numberings we refer to in the rest of this paper are the catalogue number from Hatchell et al. (2007a)

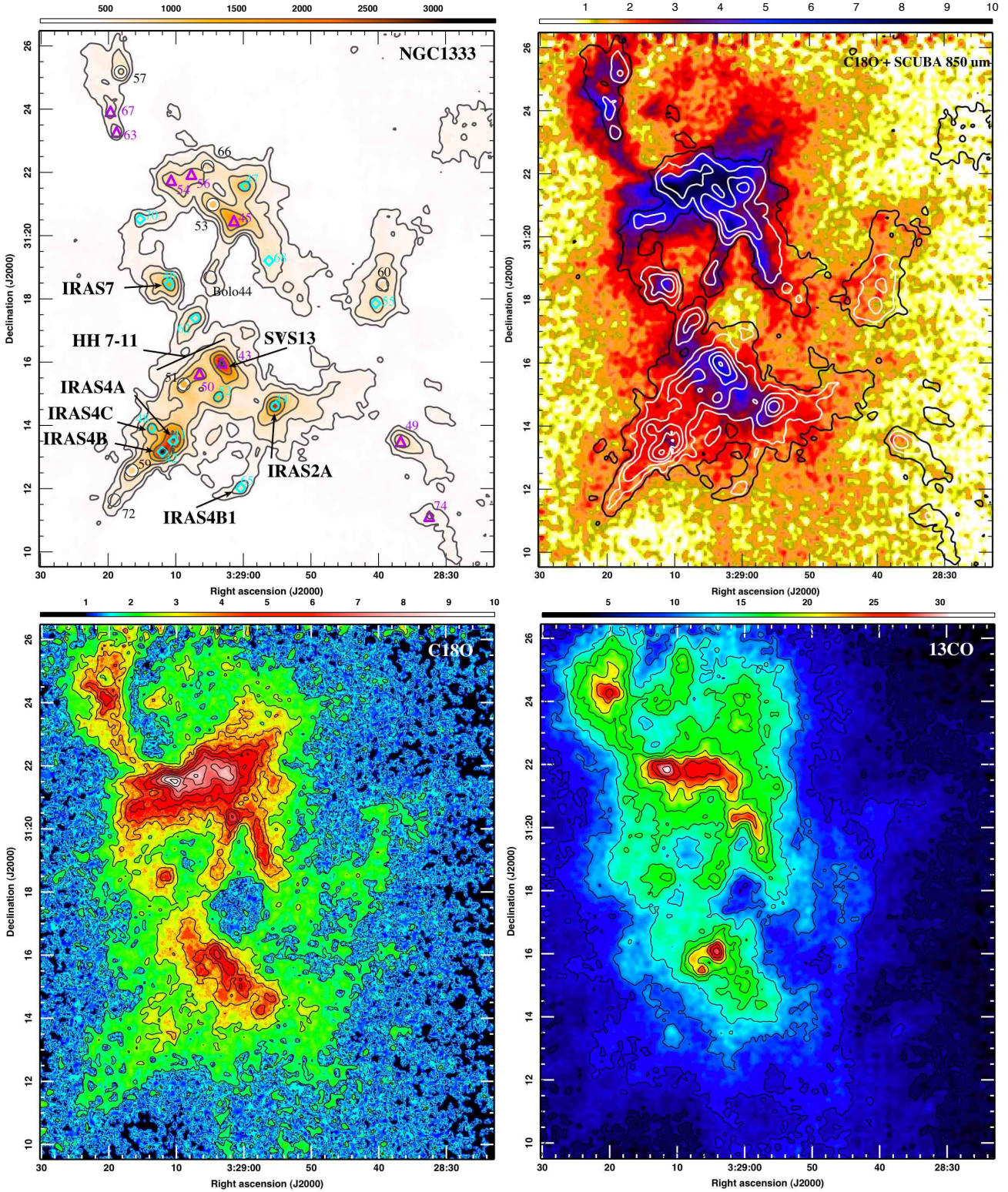


Figure 5. Overview of the data towards NGC1333. Top left: SCUBA 850 μm emission with contours at 100, 200, 400, 800, 1600 and 3200 mJy beam^{-1} (Hatchell et al. 2005) with a colour-scale as shown in mJy beam^{-1} . The peak of submillimetre cores identified and classified by Hatchell et al. (2007a) are labelled with their Hatchell et al. source number and marked with: black and white circle (starless cores), light blue diamonds (Class 0 protostars) or purple triangles (Class I protostars). Sandell & Knee (2001) originally presented this data and located many submillimetre sources. Additionally labelled are prominent sources in the field, NGC1333-IRAS2A (Jennings et al. 1987; Blake et al. 1995; Looney, Mundy & Welch 2000), NGC1333-IRAS4A to C (Jennings et al. 1987; Lay, Carlstrom & Hills 1995; Rodríguez, Anglada & Curiel 1999; Looney et al. 2000), SVS13 (Strom, Vrba & Strom 1976; Haschick et al. 1980; Snell & Edwards 1981; Grossman et al. 1987; Hirota et al. 2008), HH7-11 (Herbig 1974) and NGC1333-IRAS7 (Lightfoot & Glencross 1986; Jennings et al. 1987; Cohen, Jones & Hereld 1991; Jørgensen et al. 2007b). Top right: Contours of SCUBA 850 μm emission (as previously) overlaid on the $\text{C}^{18}\text{O } J=3 \rightarrow 2$ integrated intensity as displayed on the bottom left. Bottom left: Integrated $\text{C}^{18}\text{O } J=3 \rightarrow 2$ intensity, $\int T_{\text{A}}^* dv$, from 5 to 10 km s^{-1} with contours from 1 to 10 K km s^{-1} in steps of 1 K km s^{-1} . Bottom right: Integrated $^{13}\text{CO } J=3 \rightarrow 2$ intensity, $\int T_{\text{A}}^* dv$, from 2 to 17 km s^{-1} with contours from 3 to 33 K km s^{-1} in steps of 3 K km s^{-1} .

or that the ^{12}CO emission comes from the protostars themselves and they are moving with respect to the ambient gas.

4.3 L1448

The dark Lynds cloud L1448 (see Fig. 7), the most westerly of our targets, is a region dominated by outflow activity. Half a dozen or so YSOs reside in its dual-core molecular structure of $\sim 100 M_{\odot}$ (Bachiller & Cernicharo 1986b; Wolf-Chase, Barsony & O’Linger 2000). Its outflows are well studied, particularly the highly-collimated, symmetric flow originating from L1448-C, one of the youngest known at the time (e.g. Bachiller et al. 1990; Bally, Lada & Lane 1993). Given that the energy in the outflows exceeds the gravitational binding energy of the cloud, L1448 is likely to be dispersed by its outflow activity (Wolf-Chase et al. 2000).

The HARP C^{18}O data seems to reflect straightforwardly the SCUBA emission in Fig. 7, with the brightest cores at $850 \mu\text{m}$ also having the greatest C^{18}O integrated intensity. Most of the SCUBA cores also appear as clumps of C^{18}O emission. The same structure is clear in ^{13}CO as well, even though there is some hint that the emission is lined up along the main southeast-northwest outflow axis. The outflows themselves dominate the ^{12}CO data with perhaps three to four flows overlapping. L1448C (source 29) drives a highly collimated outflow discovered by Bachiller et al. (1990), which was one of the highest-velocity and youngest found at the time (Bachiller et al. 1990, 1995). Its northern, blue-shifted lobe intersects an outflow from a cluster of Class 0 objects: L1448N:A/B and L1448NW. Finally, west of this cluster there are perhaps two outflows emanating from the vicinity of L1448-IRS2 (sources 30 and 31).

4.4 L1455

Our final field is towards another Lynds cloud, L1455 (Fig. 8) in the south-west of the complex with a mass of some $40\text{--}50 M_{\odot}$ (Bachiller & Cernicharo 1986a). Although the smallest and faintest of our targets, it has some of the most interesting outflow structure. The C^{18}O emission is weak and only detectable towards the handful of protostellar and starless cores in the southeast of the field. The ^{13}CO data also mainly pick out the compact sources with associated SCUBA emission. One of the brightest ^{13}CO clumps (also detected in C^{18}O at $3^{\text{h}}27^{\text{m}}33^{\text{s}}$, $30^{\circ}12'45''$) has no compact SCUBA emission and appears coincident with collimated blue-shifted emission from RNO15-FIR (L1455-FIR, source 35), a Class I source associated with the red reflection nebula of the same name. The ^{12}CO maps are more intriguing, with a prominent northwest-southeast CO outflow (Goldsmith et al. 1984; Levreault 1988) some distance from the cluster of protostars. Either this is driven by an unknown low-luminosity source or one of the known protostars. The latter explanation is promoted by Davis et al. (2008) although the structure of the outflow might suggest the former is more likely.

5 DISCUSSION

5.1 Average region properties

In Table 4, we list the masses of the regions derived from the CO isotopologues and SCUBA $850 \mu\text{m}$ data. For the continuum data, we follow Visser, Richer & Chandler (2001) in calculating the region masses, assuming a constant dust temperature and opacity of

12 K and $\kappa_{850} = 0.012 \text{ cm}^2 \text{ g}^{-1}$ respectively. The gas masses assume each spectral line is optically thin, in LTE and its emitting gas has an excitation temperature, $T_{\text{ex}} = 12 \text{ K}$. We use a standard method to derive the molecular column densities (e.g. Minchin, White & Padman 1993), which for a CO isotopologue, X, yields:

$$N(X) = 5 \times 10^{12} T_{\text{ex}} \exp\left(\frac{T_{\text{trans}}}{T_{\text{ex}}}\right) \int T_{\text{mb}} dv \text{ cm}^{-2}, \quad (1)$$

where T_{trans} is 33.7, 31.8 and 31.6 K for the $J = 3 \rightarrow 2$ transition of ^{12}CO , ^{13}CO and C^{18}O respectively and the integral is in K km s^{-1} . To calculate total masses from the derived column densities we assume molecular abundances of 10^{-7} , 10^{-6} and 10^{-4} for C^{18}O , ^{13}CO and ^{12}CO respectively relative to neutral hydrogen. A main-beam efficiency of $\eta_{\text{mb}} = 0.66$ was used for all the isotopologues as measured during HARP’s commissioning. In each map, only positions with peak values greater than three times the average noise, $\langle \sigma_{\text{RMS}} \rangle$, have been included.

The pattern of the different masses is intriguing and *not* purely what is expected given the different optical depths of the CO isotopologues. NGC1333 clearly shows the naively-expected trend; as the CO lines become increasingly optically thick ($\text{C}^{18}\text{O} \rightarrow ^{13}\text{CO} \rightarrow ^{12}\text{CO}$), only the cloud surface layers are probed, the total emission falls and the mass decreases. The SCUBA $850 \mu\text{m}$ emission, although optically thin almost everywhere, is less sensitive than the CO observations to large-scale structure ($\gtrsim 2 \text{ arcmin}$), due to the spatial chopping in the observing technique. Therefore, it potentially misses much of the cloud mass. This simple prescription is not followed in any of the other regions, except perhaps L1455. However, here the C^{18}O emission is particularly weak so most of the spectra have peaks $< 3\sigma_{\text{RMS}}$ and are therefore not included in the mass estimates of Table 4, which probably relate to three or four cores. This is a potential reason why the C^{18}O mass is so much smaller than that from SCUBA. IC348 and L1448 make an interesting contrast: the C^{18}O and ^{13}CO masses are not very different, with the ^{13}CO mass marginally larger in both cases, implying the ^{13}CO gas is probably optically thin and more widespread than the C^{18}O . However, L1448 has a SCUBA mass some 3–4 times larger than these gas estimates in contrast to IC348 whose SCUBA mass is 2–3 times smaller. C^{18}O excitation effects may explain the large C^{18}O mass in IC348, if there is a significant amount of subthermal excitation, the C^{18}O emission for a given quantity of gas would be boosted relative to LTE causing an over-estimate of the C^{18}O mass. In L1448, the small C^{18}O mass is unlikely to be caused by subthermal excitation and probably arises from a different gas-to-dust ratio or if we underestimate the dust temperature (which in any case will vary from our constant assumption of 12 K). In Section 5.3, we show the dust temperature in L1448 is always higher than the excitation temperature of the gas. If we underestimate the dust temperature then we overestimate the corresponding dust mass, which may account for some of the discrepancy between the tracers.

Average spectra in the different regions are plotted in Fig. 9. All three isotopologues are centred at similar velocities, approximately 7.8, 8.8, 4.3 and 5.0 km s^{-1} for NGC1333, IC348, L1448 and L1455 respectively. The strength of the lines are in order of their abundance as we would expect and these averages show no *global* evidence for multiple components or self-absorption. However, individual ^{12}CO spectra *do* show self-absorption and/or multiple components. In L1448, the ^{13}CO line is nearly the same strength as the ^{12}CO , implying the ^{12}CO line is either saturated (and therefore the gas has a low physical temperature) or there are significant optical depths in the ^{12}CO gas due to density or tem-

Table 4. Region masses from the various HARP $J = 3 \rightarrow 2$ integrated intensities and SCUBA 850 μm emission. All spectral-line estimates assume LTE, $\tau \ll 1$ and $T_{\text{ex}} = 12$ K, while the SCUBA estimate assumes a constant dust temperature of 12 K. Only points with peaks $> 3(\sigma_{\text{RMS}})$ have been included.

Region	Masses (M_{\odot})			
	850 μm	C^{18}O	C^{13}CO	C^{12}CO
NGC1333	250	412	301	13
IC348	71	160	212	35
L1448	153	38	45	9
L1455	45	7	35	12

perature effects. Finally, even an average C^{12}CO spectrum contains significant high-velocity linewings and there are weaker linewings clear in the C^{13}CO spectra towards L1448 and IC348.

C^{18}O is an ideal tracer of the bulk motions of the molecular gas, given that it is nearly optically thin throughout and detectable over larger areas than denser-gas tracers. We plot C^{18}O line centres across the regions in Fig. 10. The centres are from non-linear least squares fitting of Gaussian functions to every spectrum with a peak $> 3\sigma_{\text{RMS}}$ (the noise calculated on each individual spectrum), performed using software from S. Graves. There are many plausible explanations for variations in velocity across a cloud region:

(i) *Rotation.* A systematic shift in the line velocity along a particular direction is often suggested to be a signature of bulk rotation. For instance the Serpens cloud core is thought to be undergoing a global east to west rotation (e.g. Olmi & Testi 2002) which manifests itself in a very ordered change in the $\text{C}^{18}\text{O } J = 3 \rightarrow 2$ velocity observed with HARP by the GBS (Graves et al., in preparation). In the Perseus regions there are few such global gradients. Ho & Barrett (1980) inferred a south to north rotation of NGC1333 from NH_3 observations, although Walsh et al. (2007) (and this work) find no such *global* gradient in N_2H^+ , suggesting Ho & Barrett were biased by the red-shifted gas around IRAS7 (in the centre-left of our map).

(ii) *Outflows.* On large scales in our fields, CO outflows do not seem to correlate with the C^{18}O centres (although there is some link on the scale of individual cores; Curtis & Richer, in preparation).

(iii) *Constituent clumps moving with respect to the bulk cloud.* Example SCUBA cores seem to enclose regions of very different velocity, which implies some of the variations trace clumps of gas that move at distinct velocities with respect to the ambient cloud.

(iv) *Gas Flows.* In a similar fashion to (iii) the variations in velocity could reflect larger flows of gas. In gravoturbulent models we expect cores to form at stagnation points, where convergent streams of material collide (e.g. Padoan et al. 2001). In these data, there are large areas of coherent motion but the cores do not seem to occur solely where they intersect.

5.2 $\text{C}^{13}\text{CO}/\text{C}^{18}\text{O}$ ratio

The optical depth of a spectral line provides important evidence as to where in the cloud it has been emitted. Optically-thin molecular lines can provide a trustworthy measure of the column density and conditions throughout the cloud, whereas optically-thick lines saturate, only tracing the outer layers. From the peak $\text{C}^{13}\text{CO}/\text{C}^{18}\text{O}$ ratio, we can get a measure of the optical depth of the $\text{C}^{18}\text{O } J = 3 \rightarrow 2$ line in the densest region along the line of sight and thereby test its fidelity as a total mass tracer.

Using the radiative transfer equation for an isothermal slab (see e.g. Rohlfs & Wilson 2004), we can relate the $\text{C}^{13}\text{CO}/\text{C}^{18}\text{O}$ intensity ratio at the velocity of the peak of the C^{18}O line, R , to the optical depths of both species (τ_{13} and τ_{18} respectively), assuming both transitions are at the same frequency, emanating from the same volume of material and have the same η_{mb} and beam-filling factors:

$$R = \frac{T_{\text{A}}^*(\text{C}^{13}\text{CO})}{T_{\text{A}}^*(\text{C}^{18}\text{O})} = \frac{1 - \exp(-\tau_{13})}{1 - \exp(-\tau_{18})}. \quad (2)$$

The opacities are expected to be linked through the abundance of C^{13}CO relative to C^{18}O , which we denote ζ , as $\tau_{13} = \zeta \tau_{18}$ (e.g. Myers, Linke & Benson 1983). Where the lines (particularly of C^{13}CO) are optically thin, $\tau \rightarrow 0$, and $R \rightarrow \zeta$ asymptotically. The absolute values of the C^{13}CO and C^{18}O abundances are not known to high precision and may differ across regions or between clouds, due to statistical variations across the Galaxy. For instance in photon dominated regions, R can be very high where there is little self-shielding of the cloud from incident radiation, causing the rarer isotopologue to be almost completely destroyed (Störzer et al. 2000). Wilson & Rood (1994) collated various studies together and tracked the changes in relative abundances with distance from the Galactic centre. In the local interstellar medium they found $[\text{C}^{12}]/[\text{C}^{13}] = 77 \pm 7$ and $[\text{O}^{16}]/[\text{O}^{18}] = 560 \pm 25$, indicating $\zeta = 7.3 \pm 0.7$ if there is no fractionation.

In calculations of R , we only include points that have a good detection of both the C^{18}O and C^{13}CO lines (peak line brightness > 5 times the RMS spectral noise). We plot R in Fig. 11. Where the gas becomes less dense R tends to ζ . In Fig. 11, outside of the SCUBA contours, so presumably at lower space densities, the ratio is ~ 5 – 6 . At the very edges of the measured values in NGC1333 and IC348, R reaches ~ 7 – 8 , the value from Wilson & Rood (1994) and becomes larger still. These larger ratios could either be a result of actual deviations in ζ or from noise effects. Most of the largest R are in the northeast of NGC1333 and northeast of the main horseshoe of SCUBA emission in IC348. These two areas are not representative of the two regions. In NGC1333, this is where a bubble of bright 8.0 μm *Spitzer* flux resides (see fig. 1 of Gutermuth et al. 2008), commonly thought to be emission from polycyclic aromatic hydrocarbon features excited by UV radiation. The UV source is likely to heat up the molecular gas in the region and perhaps change the isotopologues' abundances. In the IC348 area, there is a mass of blue-shifted C^{12}CO gas, expanding into a dust cavity (Tafalla et al. 2006 and Curtis et al., in preparation). Thus, disregarding these areas, $R \rightarrow \sim 7$ at the edges of the map, which we take to be ζ in the following analysis.

For $\zeta = 7$, $\tau_{13} = 7\tau_{18}$ and R varies with τ as in Fig. 12. R clearly falls towards the centre of the dust filaments and cores, where we expect the gas to be more dense. The average R in each region is unlikely to relate convincingly the properties of the whole area as it is measured over such a small portion of the maps, particularly in L1448 and L1455. The typical ratios can be measured in the majority of the star-forming SCUBA cores, which may prove more informative. We measured R at the peak of each core identified by Hatchell et al. (2007a) and present their averages with those in the entire regions for comparison in Tables 5 and 6.

The typical ratios across the four regions, $R \approx 2$ – 4 , translate into $\tau_{13} \approx 1.52$ – 0.15 and $\tau_{18} \approx 0.22$ – 0.02 . This suggests that the C^{18}O line is typically optically thin but the C^{13}CO can be classed neither as optically thin nor thick. The pattern of R suggests that on average L1448 has the highest column density, followed by NGC1333, whilst IC348 has the smallest. The value for L1455 is

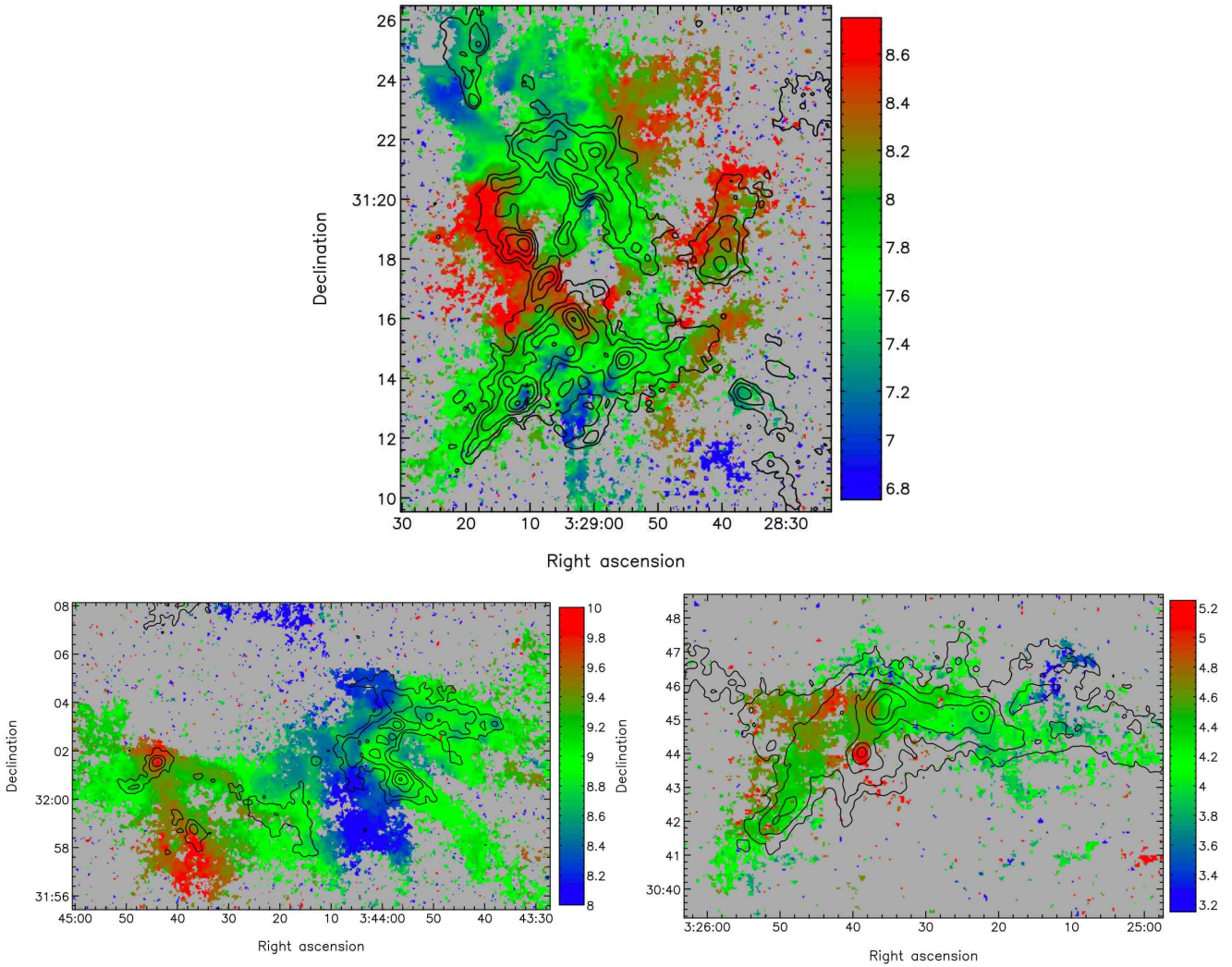


Figure 10. Motions along the line of sight in our target fields, NGC1333 (top), IC348 (bottom left) and L1448 (bottom right). At each point where the C^{18}O $J = 3 \rightarrow 2$ line has a peak greater than $\text{C}^{18}\text{O} > 3\sigma_{\text{RMS}}$ the line centre velocity (in km s^{-1}) is plotted. The line centres have been computed by fitting a single Gaussian to the spectrum at each point. L1455 did not have strong enough C^{18}O emission for such fitting.

Table 5. $^{13}\text{CO}/\text{C}^{18}\text{O}$ ratios, R , at the peak of the SCUBA cores in the Hatchell et al. (2007a) catalogue. σ_R is the standard deviation of R across the cores.

Region or Core Class	Number	$\langle R \rangle$	σ_R
NGC1333	28	2.8	0.8
IC348	16	3.0	0.8
L1448	7	2.2	0.3
L1455	1	3.6	–
Starless	21	2.8	0.6
Class 0	21	2.6	0.8
Class I	10	3.1	1.0

not representative of the region as it is only measured in the dense cores. When just the cores are examined the pattern is the same IC348 has the largest R followed by NGC1333 and then L1448. As we expect, the cores have larger optical depths than their parent clouds on average. However, the reduction in R is not enough to render the core C^{18}O gas optically thick. The *smallest* core ratio

Table 6. $^{13}\text{CO}/\text{C}^{18}\text{O}$ ratios, R , for every map pixel in Fig. 11 σ_R is the standard deviation of R across the pixels.

Region	$\langle R \rangle$	σ_R	Median R
NGC1333	3.7	1.3	3.5
IC348	4.1	1.8	3.6
L1448	2.8	0.7	2.7
L1455	3.6	0.9	3.8

is 1.62 in NGC1333, which implies $\tau_{18} \approx 1.0$ whereas most cores have much smaller τ_{18} . The mean core ratios are smaller (and thus the column densities are higher) for Class 0 than I protostars, although there is significant spread in both populations. As collapse progresses in protostars, they accrete an increasing fraction of their envelopes on to the central object so reducing the column density seen towards Class I over 0 cores. The column density seen towards starless cores presumably depends on the exact age of the core so could be comparable to the protostars' or entirely different.

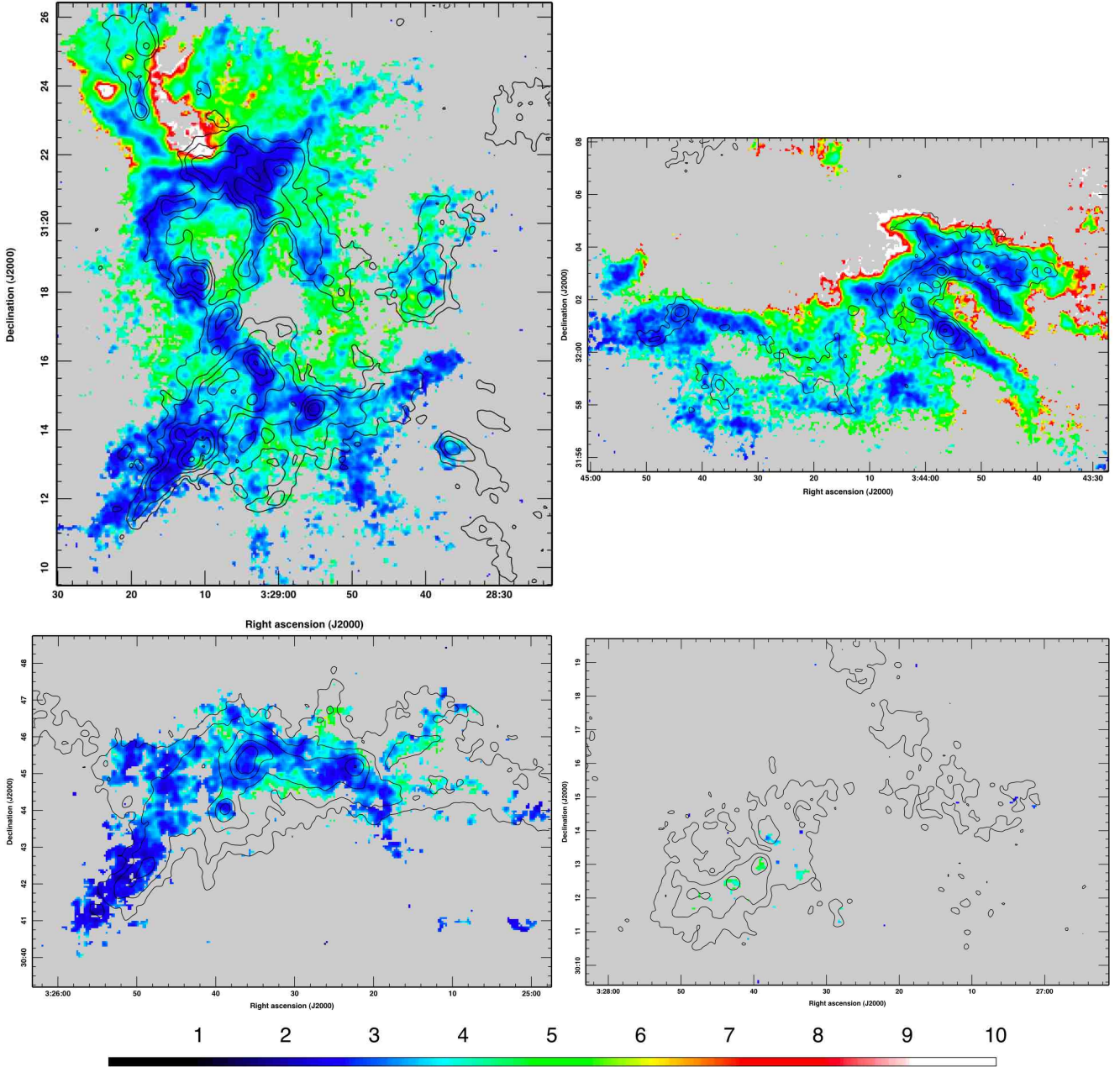


Figure 11. Ratio of the ^{13}CO to C^{18}O antenna temperatures (R) measured at the C^{18}O line peak in NGC1333 (top left), IC348 (top right), L1448 (bottom left) and L1455 (bottom right). Pixels are only displayed where both isotopologues have peak intensities $> 5\sigma_{\text{RMS}}$. Contours as in Fig. 10.

5.3 Temperature

In this section, we derive T_{ex} for the $^{12}\text{CO } J = 3 \rightarrow 2$ line assuming it is optically thick. We include ^{12}CO HARP data for NGC1333 over the region observed in $^{13}\text{CO}/\text{C}^{18}\text{O}$ (J. Swift, personal communication) which are distributed on a coarser grid of 6 arcsec pixels using a nearest-neighbour scheme.

In LTE, T_{ex} is the physical temperature of the gas, although this will of course not be the case in general. We have noted typical ^{13}CO optical depths of $\tau_{13} \approx 1 - 2$, which provided the abundance $[\text{C}^{13}]/[\text{C}^{12}] = 77$ (Wilson & Rood 1994) should ensure the opacity of the ^{12}CO gas is $\tau_{12} \approx 77 - 154$. Ratio maps with other isotopologues for ^{12}CO are unlikely to produce accurate τ_{12} values as ^{12}CO traces outer cloud layers and not the volumes where

$^{13}\text{CO}/\text{C}^{18}\text{O}$ are emitted. However, provided the line is optically thick, i.e. $\tau \rightarrow \infty$, and not self-absorbed, we can derive T_{ex} thus (see e.g. Pineda et al. 2008):

$$T_{\text{ex}}(^{12}\text{CO}) = \frac{16.59 \text{ K}}{\ln \left\{ 1 + 16.6 \text{ K} / [T_{\text{max}}(^{12}\text{CO}) + 0.036 \text{ K}] \right\}} \quad (3)$$

where $T_0 = 16.59 \text{ K}$ and $T_{\text{max}}(^{12}\text{CO})$ is the peak ^{12}CO main beam brightness temperature. We plot T_{ex} in Figs. 13 and 14. T_{ex} is typically 5–25 K, generally increasing towards the centre of each region where it can reach 30 K.

There are a number of caveats to this analysis that should be noted. First, in some respects the most interesting regions of molecular clouds are the cores in which stars are formed. The tempera-

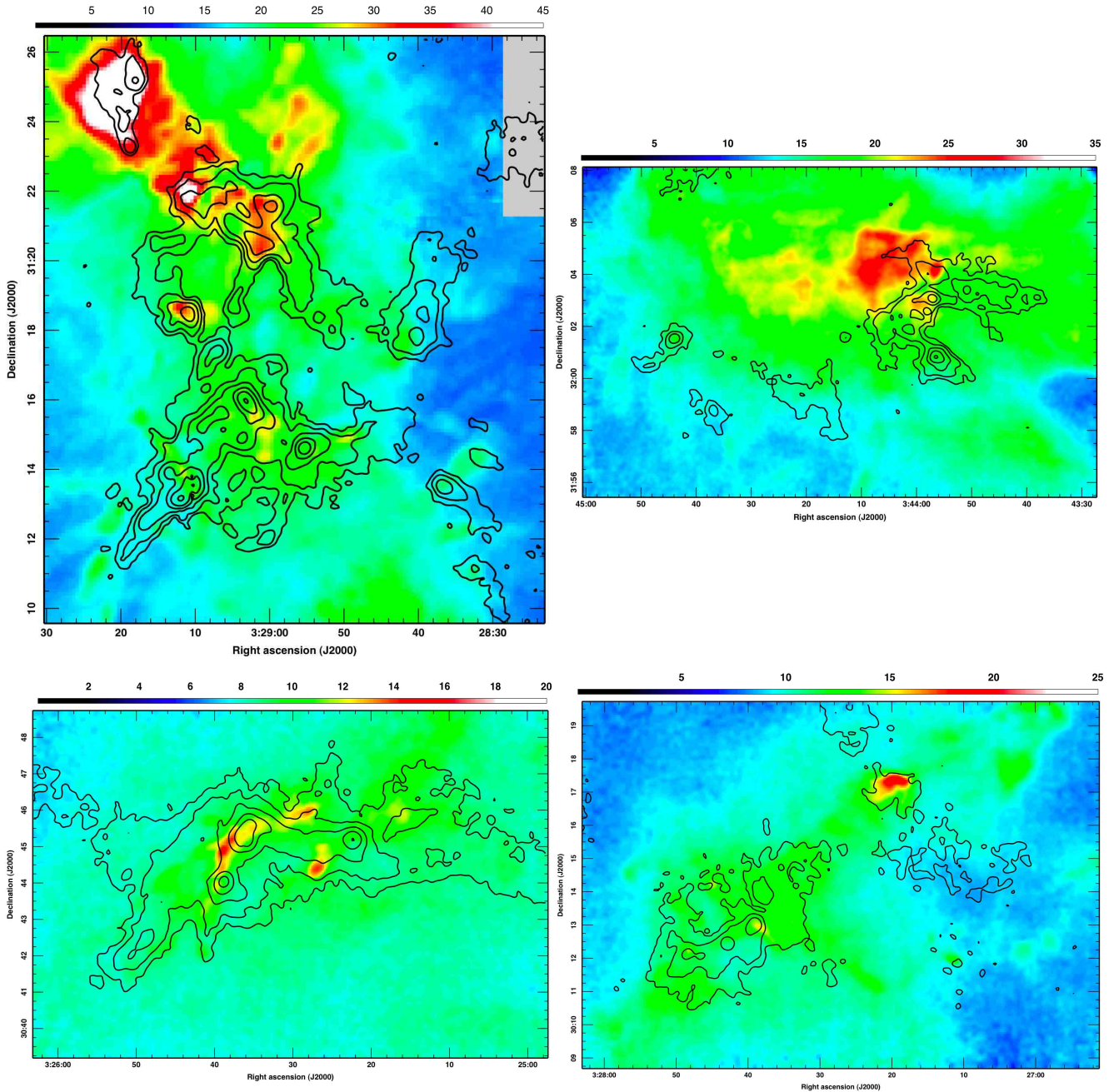


Figure 13. T_{ex} in K derived from the peak ^{12}CO main beam brightness temperature with panels as arrange in Fig. 11. Contours as in Fig. 10.

tures of such high-density regions will not be accurately probed by ^{12}CO , whose emission is restricted to outer cloud material due to its higher opacity. However, we might naturally expect the temperature of starless cores (without an internal heating source) and possibly protostars to reflect that of their natal environment so the ^{12}CO temperature should reflect the pattern of core conditions. Second, ^{12}CO may not be optically thick everywhere, although the typical ^{13}CO optical depths in regions with bright SCUBA emission do suggest it will be for most of the areas. Furthermore, we may underestimate the true ^{12}CO peak temperature if the line profile is complicated by effects such as infall and self-absorption.

In L1455, L1448 and IC348, the T_{ex} maps follow the integrated ^{12}CO intensities closely. Any strong outflows are promi-

nent areas of higher T_{ex} , as suggested by other authors (Hatchell, Fuller & Ladd 1999; Nisini et al. 2000). The dominant feature in NGC1333's T_{ex} map is the blue-shifted bubble of gas in the north-east corner. We have already mentioned this is an area likely to be illuminated by a UV source. By contrast, the most pronounced feature in the ^{12}CO integrated intensity, the bright outflow from SVS13, is almost absent. The bubble's T_{ex} is some 40 K higher than the maximum in the other regions. In this part of the map, ^{12}CO is not optically thick and the gas probably has a higher physical temperature – as we noted the $^{13}\text{CO}/\text{C}^{18}\text{O}$ ratio is larger in this region. Additionally, it only has single-peaked lines, devoid of some of the more complicated profiles seen in NGC1333, suggesting its peak temperature is over-estimated compared to the rest of the cloud.

Table 7. T_{ex} from ^{12}CO at the peak of the SCUBA cores in the Hatchell et al. (2007a) catalogue by region or source age.

Region or Core Class	Number	$\langle T_{\text{ex}} \rangle / \text{K}$	σ_T / K
NGC1333	29	25.2	10.1
IC348	17	17.6	3.2
L1448	7	10.6	2.0
L1455	5	12.6	2.2
Starless	23	18.8	9.7
Class 0	21	18.3	6.2
Class I	14	24.9	11.2

This all points to a warm, low-density region with material perhaps dispersed by nearby luminous stars, which Hatchell, Fuller & Richer (2007b) suggest are the cause of a lack of outflow detections in this area.

It is interesting that the largest temperatures in NGC1333 are to the northeast, in the direction of 40 Persei ($03^{\text{h}}42^{\text{m}}22.6^{\text{s}}, +33^{\circ}57'54.1''$), a B0.5 star, part of the Perseus OB association, suggested to be triggering the star formation in these clouds (Walawender et al. 2004; Kirk et al. 2006). Indeed, the highest temperatures are to the north in IC348, also in the direction of 40 Per, although no such gradients are clear in L1448 and L1455, possibly as they are further away.

On average, L1448 is the coldest, followed in order of increasing temperature by L1455 then IC348, with NGC1333 the hottest. The histograms of Fig. 14 show two distinct temperature environments: one colder in L1455 and L1448 and the other hotter in IC348 and NGC1333. The latter two regions show a large range of temperatures. NGC1333 and IC348 are probably heated more by their namesake IR clusters and the triggering radiation from 40 Per than L1448 and L1455. Protostars may also heat their surroundings to a limited extent via radiation and outflows. NGC1333 with its numerous energetic flows and protostars is most likely to be warmed up in this way. L1448 has a high protostellar fraction as well and powerful outflows but less ambient gas with which to interact – most of the outflows have broken out of the region.

As we have already mentioned, temperatures derived from ^{12}CO are unlikely to be best probes of conditions inside dense cores. Nevertheless we might expect the core temperatures to be affected to some extent by the temperature in the bulk of the gas. From Table 7, it is clear the temperatures towards the cores are larger on average than within their parent region as a whole but exhibit the same trends. When comparing cores of different ages it is worth noting that we expect fundamentally different relations between T_{ex} and the true temperatures for starless and protostellar cores, T_{core} . Towards the centres of starless cores, temperatures fall whereas for protostars temperatures rise. Thus, for starless cores $T_{\text{ex}} > T_{\text{core}}$ and for protostars $T_{\text{ex}} < T_{\text{core}}$. In Table 7 the *environments* of Class I protostars appear slightly warmer than both starless cores and Class 0 protostars on average. As a source ages we expect its core temperature to increase, resulting from the increase in brightness of its central object. These data would exhibit this trend except the Class 0 and starless cores have similar temperatures, probably illustrating that the ^{12}CO line probes an environment outside the high-density core, where $T_{\text{ex}} > T_{\text{core}}$ for the starless cores and $T_{\text{ex}} < T_{\text{core}}$ for the protostars.

We can make an interesting comparison between this gas temperature and that of the dust. At high densities, $n \gtrsim 2 \times 10^4 \text{ cm}^{-3}$, conditions likely to be probed in CO with HARP, the gas and dust

temperatures are coupled (Galli, Walmsley & Gonçalves 2002). Recently, Schnee et al. (2008) computed the dust temperature at 40 arcsec resolution across Perseus using *Spitzer* and *IRAS* measurements. We plot T_{ex} degraded to 40 arcsec resolution versus Schnee et al.'s dust temperature in Fig. 15. The dust temperature, T_{D} , was calculated from *Spitzer* 70 and 160 μm fluxes, which is dominated by warm dust along the line of sight rather than the denser, colder material in say starless cores and is more likely to match the material traced in ^{12}CO . There is actually little correlation between the two temperatures. Typically T_{D} is slightly lower than T_{ex} : 12–20 K compared to 8–30 K. In NGC1333 and IC348, T_{ex} is mostly larger than T_{D} although there is a significant proportion of pixels where the opposite is true. However, in L1448 and L1455, nearly everywhere $T_{\text{D}} > T_{\text{ex}}$. This may be explained if the ^{12}CO gas is not tracing the same areas as the dust emission, with the ^{12}CO emitted in a colder layer whilst the dust comes from a hotter inner cloud region. Additionally, if the gas is not optically thick, then we would over-estimate the ^{12}CO excitation temperature and $T_{\text{ex}} > T_{\text{D}}$.

The ^{12}CO excitation temperature may be correlated with the cloud column density. As the rotational transition is collisionally excited, on moving to denser and higher extinction portions of the cloud with densities above the critical density, the gas T_{ex} should increase. We use the integrated $\text{C}^{18}\text{O } J = 3 \rightarrow 2$ intensity as a proxy for the visual extinction since typically there is a linear relation between them. Using $\text{C}^{18}\text{O } J = 1 \rightarrow 0$ data across the Perseus molecular cloud Pineda et al. (2008) measured:

$$A_{\text{v}} / \text{mag} = (2.4 \pm 0.1) \left(\frac{\int T_{\text{mb}}(\text{C}^{18}\text{O}) \text{d}v}{\text{K km s}^{-1}} \right) + (2.9 \pm 0.9). \quad (4)$$

In Fig. 15, we plot the C^{18}O integrated intensity, $\int T_{\text{A}}^* \text{d}v$ versus T_{ex} , with lines denoting the expected variation for various column densities of C^{18}O assuming LTE. No single line is a good fit for all the points as in each region there is a range of column densities. However, a moderate range of column densities will span the whole parameter space. At low temperatures with a good deal of scatter the integrated intensity increases linearly with T_{ex} . L1448 again requires the highest column densities with IC348 and NGC1333 having a large spread in conditions.

6 SUMMARY

This paper presents the technical details and preliminary analysis of a large-scale survey of the kinematics of molecular gas in the Perseus molecular cloud. Observations of the $J = 3 \rightarrow 2$ rotational transitions of ^{12}CO , ^{13}CO and C^{18}O in over 600 arcmin² of NGC1333, IC348, L1448 and L1455 were undertaken with HARP on the JCMT. We introduce a new ‘flatfield’ procedure to account for striping artefacts in HARP scan maps of molecular clouds, apparently resulting from differential performance across the detectors and/or their samplers. The data from each working detector is multiplied by a conversion factor which scales its intensity to match the nominated reference detector. The factors are computed from the scientific observations themselves by calculating the total intensity received by each detector across the whole map.

We compare integrated intensity maps of the three tracers to SCUBA 850 μm emission (Hatchell et al. 2005) and the position of protostars and starless cores (Hatchell et al. 2007a) in each field. There is a striking similarity between the SCUBA maps and C^{18}O emission, hinting that similar densities of material are traced with the gas and dust strongly coupled. However, the detailed structure

of individual star-forming cores is not always so simple, for example very bright SCUBA cores sometimes have only weak C¹⁸O emission and vice versa. Many outflows are obvious in the ¹²CO data, which we will examine in detail in a subsequent study (Curtis et al. in preparation). The ¹³CO maps are somewhat intermediate between the other two isotopologues and average spectra across the maps do show weak linewings from outflows. Intriguingly, masses derived from the HARP and SCUBA data exhibit different trends across the four regions, emphasizing the need to examine the detailed excitation conditions across regions rather than simple constant assumptions.

From the ¹³CO/C¹⁸O integrated line ratio, R , we explore variations in the gas opacity and estimate the two species' relative abundance ($[^{13}\text{CO}]/[^{18}\text{O}] \sim 7$). Across most of the regions the C¹⁸O gas is optically thin ($\tau_{18} = 0.02 - 0.22$) and therefore is a reliable total mass tracer. Indeed, inside the denser parts of the clouds, the star-forming cores, the opacity does not increase beyond a maximum, $\tau_{18} = 0.9$. When we also consider that the critical density of the transition is some 10^4 cm^{-3} , we expect to probe an intermediate region between a dense core and its envelope with the C¹⁸O line. The ¹³CO optical depths are neither in the optically thin nor thick regimes (τ_{13} is typically 0.15–1.52). Class 0 protostars have smaller ratios than Class Is as expected as more material accretes on to the central object over time.

If we assume the ¹²CO line is optically thick, an estimate of the excitation temperature can be gathered from the peak line temperature, assuming LTE (in which case T_{ex} is the physical gas temperature). In general we derive temperature of 5–25 K, increasing towards the centres of the individual regions and in outflow lobes. An area in the northwest of NGC1333 has temperatures of over 45 K, probably as it is heated by a UV source and/or the region has lower density so is not optically thick. IC348 and NGC1333 are on average much warmer than L1448 and L1455. This is partly as the averages for NGC1333 are skewed upwards because of the warm gas in the north and perhaps since NGC1333 and IC348 are closer to 40 Per (thought to be triggering star formation in Perseus). There is little correlation between T_{ex} and the dust temperature, T_{D} , derived from *Spitzer* observations (Schnee et al. 2008). Typically T_{D} is slightly lower than T_{ex} : 12–20 K compared to 8–30 K. However, in L1448 and L1445, typically $T_{\text{ex}} < T_{\text{D}}$, this may imply we are tracing completely different regions with the ¹²CO gas and warm dust or that the gas is not optically thick, so we are over-estimating T_{ex} .

This work demonstrates the utility of HARP for large-scale surveys of gas kinematics in nearby molecular clouds. The $J = 3 \rightarrow 2$ transitions of CO and its isotopologues are powerful probes of the conditions of star formation when used in combination, examining moderately high densities comparable to the dust densities seen by SCUBA.

7 ACKNOWLEDGMENTS

EIC thanks the Science and Technology Facilities Council (STFC) for studentship support while carrying out this work. The authors thank Jonathan Swift for use of the ¹²CO data towards NGC1333 in advance of publication. We are also grateful to the referee, whose useful comments and suggestions significantly improved the clarity of this paper. The JCMT is operated by The Joint Astronomy Centre (JAC) on behalf of the STFC of the United Kingdom, the Netherlands Organisation for Scientific Research and the National Research Council (NRC) of Canada. We have also made exten-

sive use of the SIMBAD data base, operated at CDS, Strasbourg, France. We acknowledge the data analysis facilities provided by the Starlink Project which is maintained by JAC with support from STFC. This research used the facilities of the Canadian Astronomy Data Centre operated by the NRC with the support of the Canadian Space Agency.

REFERENCES

- Bachiller R., Cernicharo J., 1986a, *A&A*, 166, 283
 Bachiller R., Cernicharo J., 1986b, *A&A*, 168, 262
 Bachiller R., Martin-Pintado J., Tafalla M., Cernicharo J., Lazareff B., 1990, *A&A*, 231, 174
 Bachiller R., Guilloteau S., Dutrey A., Planesas P., Martin-Pintado J., 1995, *A&A*, 299, 857
 Ballesteros-Paredes J., Mac Low M.-M., 2002, *ApJ*, 570, 734
 Bally J., Lada E. A., Lane A. P., 1993, *ApJ*, 418, 322
 Bally J., Walawender J., Johnstone D., Kirk H., Goodman A., 2008, in Reipurth B., ed., *ASP Conf. Ser., Handbook of Star Forming Regions*. Astron. Soc. Pac., San Francisco, p. 308
 Bate M. R., 2009a, *MNRAS*, 392, 590
 Bate M. R., 2009b, *MNRAS*, 392, 1363
 Bate M. R., Bonnell I. A., 2005, *MNRAS*, 356, 1201
 Blake G. A., Sandell G., van Dishoeck E. F., Groesbeck T. D., Mundy L. G., Aspin C., 1995, *ApJ*, 441, 689
 Boulard M.-H., Caux E., Monin J.-L., Nadeau D., Rowlands N., 1995, *A&A*, 300, 276
 Buckle J. V., Hills, R. E., Smith, H. et al., 2009, *MNRAS*, in press
 Černis K., 1990, *Astrophys. and Space Sci.*, 166, 315
 Černis K., 1993, *Baltic Astron.*, 2, 214
 Černis K., Straizys V., 2003, *Baltic Astron.*, 12, 301
 Chandler C. J., Richer J. S., 2001, *ApJ*, 555, 139
 Cohen M., Jones B. F., Hereld M., 1991, *ApJ*, 371, 237
 Curiel S., Raymond J. C., Moran J. M., Rodriguez L. F., Canto J., 1990, *ApJ*, 365, L85
 Curiel S., Torrelles J. M., Rodríguez L. F., Gómez J. F., Anglada G., 1999, *ApJ*, 527, 310
 Davis C. J., Eisloffel J., Ray T. P., Jenness T., 1997, *A&A*, 324, 1013
 Davis C. J., Scholz P., Lucas P., Smith M. D., Adamson A., 2008, *MNRAS*, 387, 954
 de Zeeuw P. T., Hoogerwerf R., de Bruijne J. H. J., Brown A. G. A., Blaauw A., 1999, *AJ*, 117, 354
 Di Francesco J., Johnstone D., Kirk H., MacKenzie T., Ledwosinska E., 2008, *ApJS*, 175, 277
 Eisloffel J., Froebrich D., Stanke T., McCaughrean M. J., 2003, *ApJ*, 595, 259
 Enoch M. L., Young K. E., Glenn J. et al., 2006, *ApJ*, 638, 293
 Enoch M. L., Evans II N. J., Sargent A. I., Glenn J., Rosolowsky E., Myers P., 2008, *ApJ*, 684, 1240
 Enoch M. L., Evans II N. J., Sargent A. I., Glenn J., 2009, *ApJ*, 692, 973
 Evans II N. J., Allen L. E., Blake G. A. et al., 2003, *PASP*, 115, 965
 Evans II N. J., Dunham M. M., Jørgensen J. K. et al., 2009, *ApJS*, 181, 321
 Galli D., Walmsley M., Gonçalves J., 2002, *A&A*, 394, 275
 Goldsmith P. F., Snell R. L., Hemeon-Heyer M., Langer W. D., 1984, *ApJ*, 286, 599
 Grossman E. N., Masson C. R., Sargent A. I., Scoville N. Z., Scott S., Woody D. P., 1987, *ApJ*, 320, 356

- Gueth F., Guilloteau S., 1999, *A&A*, 343, 571
- Gutermuth R. A., Myers P. C., Megeath S. T. et al., 2008, *ApJ*, 674, 336
- Haschick A. D., Moran J. M., Rodriguez L. F., Burke B. F., Greenfield P., Garcia-Barreto J. A., 1980, *ApJ*, 237, 26
- Hatchell J., Fuller G. A., Ladd E. F., 1999, *A&A*, 344, 687
- Hatchell J., Richer J. S., Fuller G. A., Qualtrough C. J., Ladd E. F., Chandler C. J., 2005, *A&A*, 440, 151
- Hatchell J., Fuller G. A., Richer J. S., Harries T. J., Ladd E. F., 2007a, *A&A*, 468, 1009
- Hatchell J., Fuller G. A., Richer J. S., 2007b, *A&A*, 472, 187
- Herbig G. H., 1974, *Lick Obser. Bull.*, 658, 1
- Herbig G. H., Jones B. F., 1983, *AJ*, 88, 1040
- Herbst W., 2008, in Reipurth B., ed., *ASP Conf. Ser., Handbook of Star Forming Regions. Astron. Soc. Pac., San Francisco*, p. 372
- Hirota T., Bushimata T., Choi Y. K. et al., 2008, *PASJ*, 60, 37
- Ho P. T. P., Barrett A. H., 1980, *ApJ*, 237, 38
- Holland W. S., Robson E. I., Gear W. K. et al., 1999, *MNRAS*, 303, 659
- Jenness T., Cavanagh B., Economou F., Berry D. S., 2008, in Argyle R. W., Bunclark P. S., Lewis J. R., eds, *ASP Conf. Ser., Vol. 394, Astronomical Data Analysis Software and Systems XVII. Astron. Soc. Pac., San Francisco*, p. 565
- Jennings R. E., Cameron D. H. M., Cudlip W., Hirst C. J., 1987, *MNRAS*, 226, 461
- Johnstone D., Wilson C. D., Moriarty-Schieven G., Joncas G., Smith G., Gregersen E., Fich M., 2000, *ApJ*, 545, 327
- Jørgensen J. K., Harvey P. M., Evans II N. J. et al., 2006, *ApJ*, 645, 1246
- Jørgensen J. K., Johnstone D., Kirk H., Myers P. C., 2007a, *ApJ*, 656, 293
- Jørgensen J. K., Bourke T. L., Myers P. C. et al., 2007b, *ApJ*, 659, 479
- Jørgensen J. K., Johnstone D., Kirk H., Myers P. C., Allen L. E., Shirley Y. L., 2008, *ApJ*, 683, 822
- Kirk H., Johnstone D., Di Francesco J., 2006, *ApJ*, 646, 1009
- Kirk H., Johnstone D., Tafalla M., 2007, *ApJ*, 668, 1042
- Klessen R. S., Burkert A., 2000, *ApJS*, 128, 287
- Knee L. B. G., Sandell G., 2000, *A&A*, 361, 671
- Kutner M. L., Ulich B. L., 1981, *ApJ*, 250, 341
- Lada C. J., Alves J., Lada E. A., 1996, *AJ*, 111, 1964
- Ladd E. F., Lada E. A., Myers P. C., 1993, *ApJ*, 410, 168
- Lay O. P., Carlstrom J. E., Hills R. E., 1995, *ApJ*, 452, L73
- Lefloch B., Castets A., Cernicharo J., Langer W. D., Zylka R., 1998, *A&A*, 334, 269
- Levreault R. M., 1988, *ApJS*, 67, 283
- Lightfoot J. F., Glencross W. M., 1986, *MNRAS*, 221, 993
- Looney L. W., Mundy L. G., Welch W. J., 2000, *ApJ*, 529, 477
- Luhman K. L., Rieke G. H., Lada C. J., Lada E. A., 1998, *ApJ*, 508, 347
- Luhman K. L., Stauffer J. R., Muench A. A., Rieke G. H., Lada E. A., Bouvier J., Lada C. J., 2003, *ApJ*, 593, 1093
- McCaughrean M. J., Rayner J. T., Zinnecker H., 1994, *ApJ*, 436, L189
- Minchin N. R., White G. J., Padman R., 1993, *A&A*, 277, 595
- Motte F., Andre P., Neri R., 1998, *A&A*, 336, 150
- Myers P. C., Linke R. A., Benson P. J., 1983, *ApJ*, 264, 517
- Nisini B., Benedettini M., Giannini T., Codella C., Lorenzetti D., di Giorgio A. M., Richer J. S., 2000, *A&A*, 360, 297
- Olmí L., Testi L., 2002, *A&A*, 392, 1053
- Padoan P., Juvela M., Goodman A. A., Nordlund Å., 2001, *ApJ*, 553, 227
- Pineda J. E., Caselli P., Goodman A. A., 2008, *ApJ*, 679, 481
- Price D. J., Bate M. R., 2008, *MNRAS*, 385, 1820
- Quillen A. C., Thorndike S. L., Cunningham A., Frank A., Gutermuth R. A., Blackman E. G., Pipher J. L., Ridge N., 2005, *ApJ*, 632, 941
- Rebull L. M., Stapelfeldt K. R., Evans II N. J. et al., 2007, *ApJS*, 171, 447
- Ridge N. A., Schnee S. L., Goodman A. A., Foster J. B., 2006a, *ApJ*, 643, 932
- Ridge N. A., Di Francesco J., Kirk H. et al., 2006b, *AJ*, 131, 2921
- Rodríguez L. F., Anglada G., Curiel S., 1999, *ApJS*, 125, 427
- Rohlfs K., Wilson T. L., 2004, *Tools of Radio Astronomy. Springer, Berlin*
- Sandell G., Knee L. B. G., 2001, *ApJ*, 546, L49
- Schnee S., Li J., Goodman A. A., Sargent A. I., 2008, *ApJ*, 684, 1228
- Schöier F. L., van der Tak F. F. S., van Dishoeck E. F., Black J. H., 2005, *A&A*, 432, 369
- Smith H., Hills R. E., Withington S. et al., 2003, in Phillips T. G., Zmuidzinas J., eds, *Proc. SPIE Vol. 4855, Millimeter and Submillimeter Detectors for Astronomy. SPIE, Bellingham*, p. 338
- Smith H., Buckle J., Hills R. et al., 2008a, in Duncan W. D., Holland W. S., Withington S., Zmuidzinas J., eds, *Proc. SPIE, Vol. 7020, Millimeter and Submillimeter Detectors and Instrumentation for Astronomy IV. SPIE, Bellingham*, p. 24
- Smith R. J., Clark P. C., Bonnell I. A., 2008b, *MNRAS*, 391, 1091
- Snell R. L., Edwards S., 1981, *ApJ*, 251, 103
- Störzer H., Zielinsky M., Stutzki J., Sternberg A., 2000, *A&A*, 358, 682
- Strom S. E., Vrba F. J., Strom K. M., 1976, *AJ*, 81, 314
- Tafalla M., Kumar M. S. N., Bachiller R., 2006, *A&A*, 456, 179
- Visser A. E., Richer J. S., Chandler C. J., 2001, *MNRAS*, 323, 257
- Walawender J., Bally J., Reipurth B., Aspin C., 2004, *AJ*, 127, 2809
- Walawender J., Bally J., Kirk H., Johnstone D., Reipurth B., Aspin C., 2006, *AJ*, 132, 467
- Walawender J., Bally J., Di Francesco J., Jørgensen J., Getman K., 2008, in Reipurth B., ed., *ASP Conf. Ser., Handbook of Star Forming Regions. Astron. Soc. Pac., San Francisco*, p. 346
- Walsh A. J., Myers P. C., Di Francesco J., Mohanty S., Bourke T. L., Gutermuth R., Wilner D., 2007, *ApJ*, 655, 958
- Ward-Thompson D., Di Francesco J., Hatchell J. et al., 2007, *PASP*, 119, 855
- Warin S., Castets A., Langer W. D., Wilson R. W., Pagani L., 1996, *A&A*, 306, 935
- Wilking B. A., Meyer M. R., Greene T. P., Mikhail A., Carlson G., 2004, *AJ*, 127, 1131
- Wilson T. L., Rood R., 1994, *ARA&A*, 32, 191
- Wolf-Chase G. A., Barsony M., O'Linger J., 2000, *AJ*, 120, 1467

This paper has been typeset from a $\text{\TeX}/\text{\LaTeX}$ file prepared by the author.

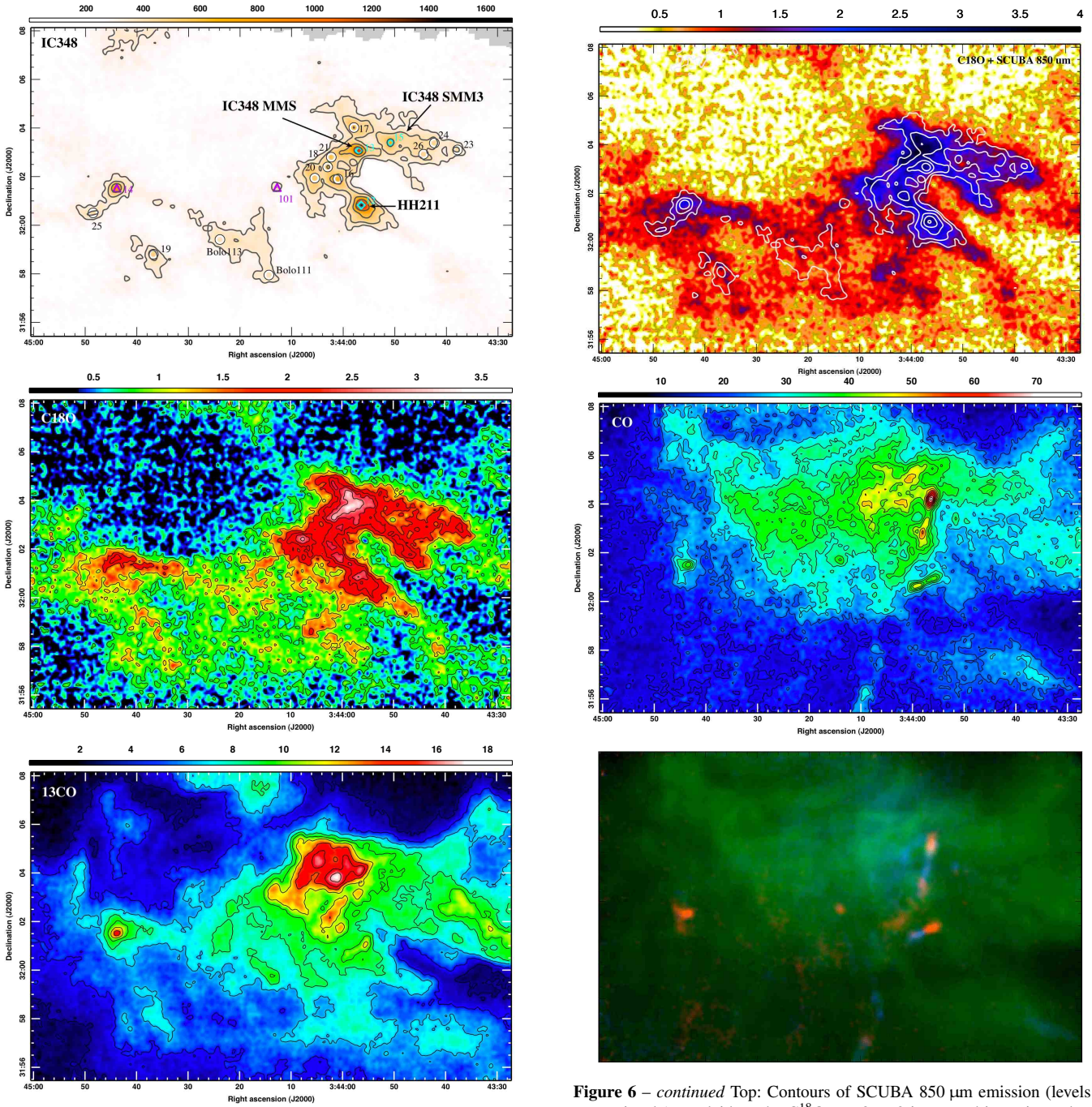


Figure 6. Overview of the data towards IC348 as for NGC1333 in Fig. 5. Top: SCUBA 850 μm emission. Prominent sources in the field are labelled: HH211 (McCaughrean et al. 1994; Gueth & Guilloteau 1999; Chandler & Richer 2001), IC348-MMS (Eisloffel et al. 2003; Tafalla et al. 2006; Walawender et al. 2006) and IC348-SMM3 (Tafalla et al. 2006). Middle: Integrated $\text{C}^{18}\text{O } J = 3 \rightarrow 2$ intensity from 7 to 10 km s^{-1} with contours from 0.5 to 3.0 K km s^{-1} in 0.5 K km s^{-1} steps. Bottom: Integrated $^{13}\text{CO } J = 3 \rightarrow 2$ intensity from 5 to 12 km s^{-1} with contours from 2 to 18 K km s^{-1} in 2 K km s^{-1} steps.

Figure 6 – continued Top: Contours of SCUBA 850 μm emission (levels as previously) overlaid on the $\text{C}^{18}\text{O } J = 3 \rightarrow 2$ integrated intensity as before. Middle: Integrated ^{12}CO intensity from 0 to 20 km s^{-1} with contours from 15 to 75 K km s^{-1} in steps of 5 K km s^{-1} . Bottom: Red-green-blue colour composite image of the mean ^{12}CO data value in various velocity ranges: from 3.5 to 5.5 km s^{-1} (blue), 7.0 to 9.0 km s^{-1} (green) and 12.0 to 14.0 km s^{-1} (red).

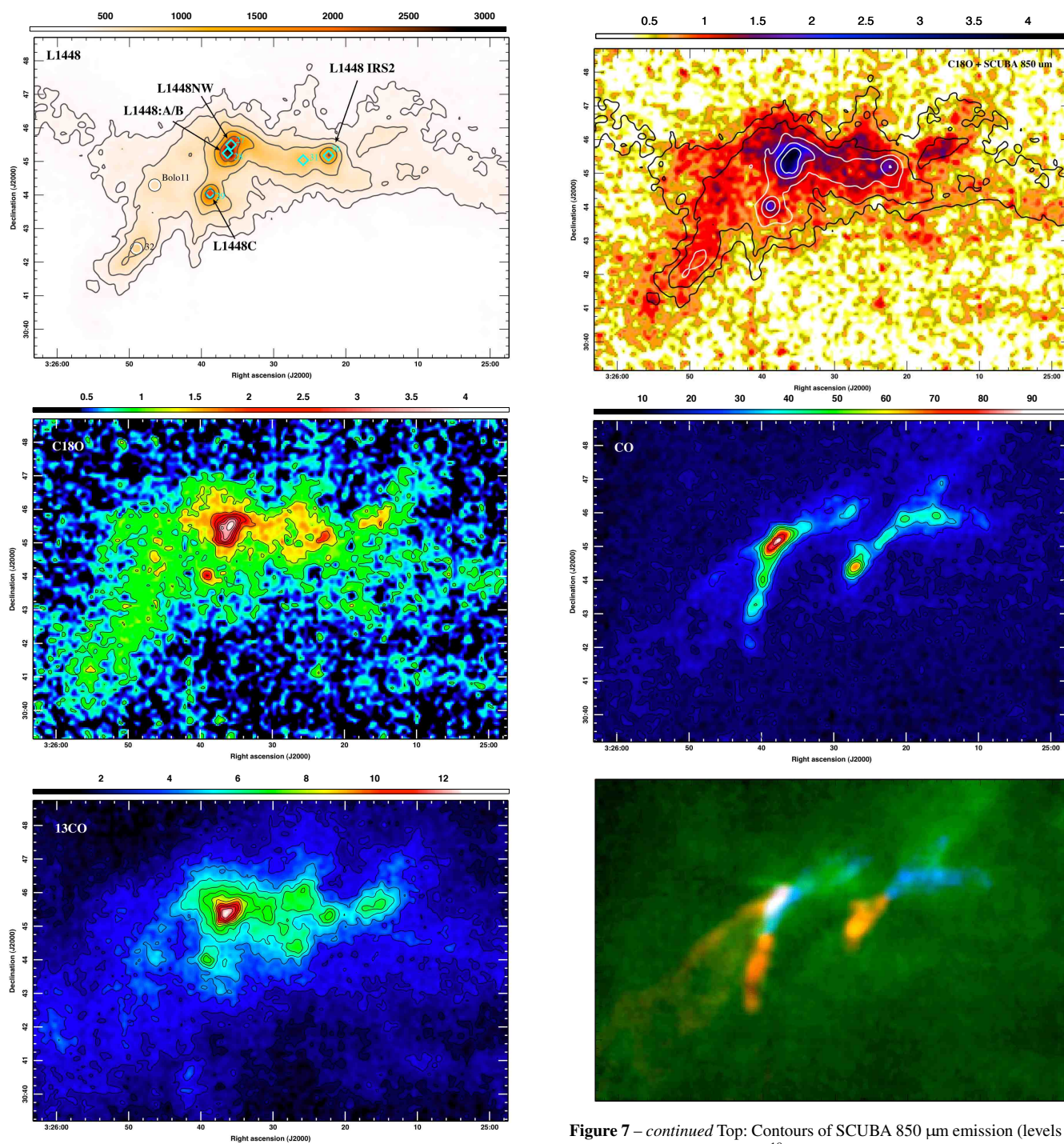


Figure 7. Overview of the data towards L1448 as for IC348 in Fig. 6. Top: SCUBA 850 μm emission. Prominent sources in the field are labelled: L1448NW, L1448:A/B (Curiel et al. 1990, 1999), L1448C (Bachiller et al. 1990, 1995) and L1448-IRS2 (Wolf-Chase et al. 2000).

Figure 7 – continued Top: Contours of SCUBA 850 μm emission (levels as previously) overlaid on the $\text{C}^{18}\text{O } J=3 \rightarrow 2$ integrated intensity as before. Middle: Integrated ^{12}CO intensity from -25 to 25 km s^{-1} with contours from 10 to 90 K km s^{-1} in steps of 10 K km s^{-1} . Bottom: Ranges: from -25 to 0 km s^{-1} (blue), 2 to 6 km s^{-1} (green) and 7 to 14 km s^{-1} (red).

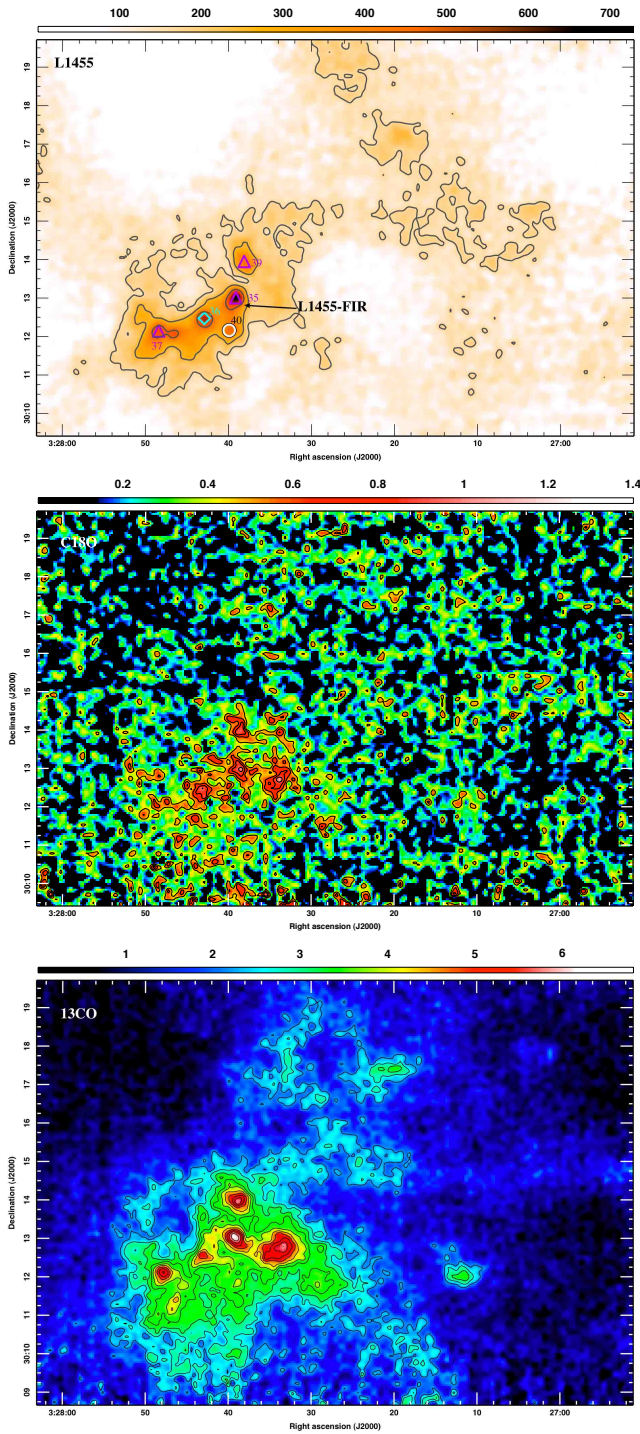


Figure 8. Overview of the data towards L1455 as for IC348 in Fig. 6. Top: SCUBA 850 μm emission. Additionally labelled is L1455-FIR (Davis et al. 1997).

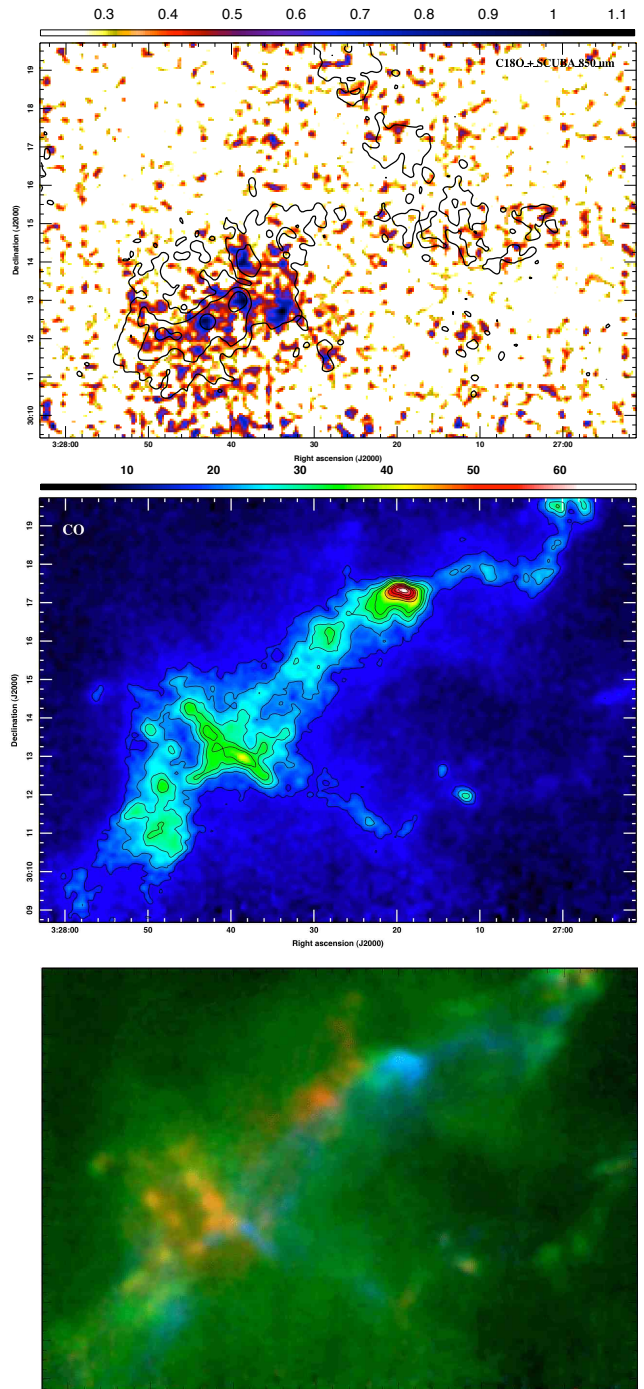


Figure 8 – continued Top: Contours of SCUBA 850 μm emission (levels as previously) overlaid on the $\text{C}^{18}\text{O } J = 3 \rightarrow 2$ integrated intensity as before. Middle: Integrated ^{12}CO intensity from -5 to 15 km s^{-1} with contours from 15 to 65 K km s^{-1} in steps of 5 K km s^{-1} . Bottom: Ranges: from -5.0 to 3.5 km s^{-1} (blue), 5.0 to 6.5 km s^{-1} (green) and 8.0 to 14.0 km s^{-1} (red).

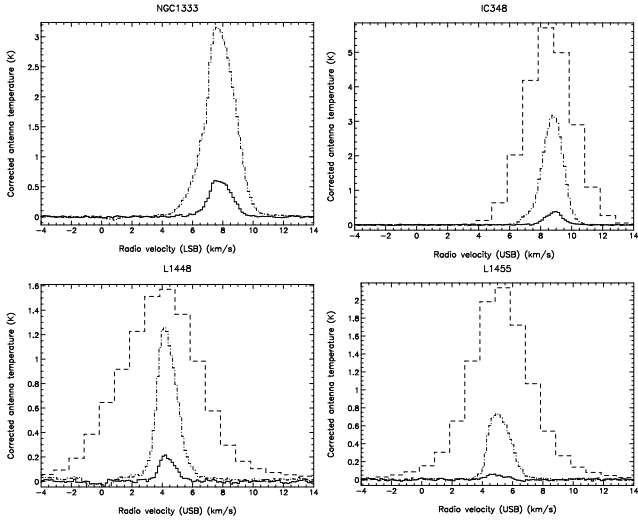


Figure 9. Average cloud spectra for the different regions. Each plot contains the averages of every spectrum in the HARP $J = 3 \rightarrow 2$ cubes: ^{12}CO (dashed), ^{13}CO (dot-dashed) and C^{18}O (solid).

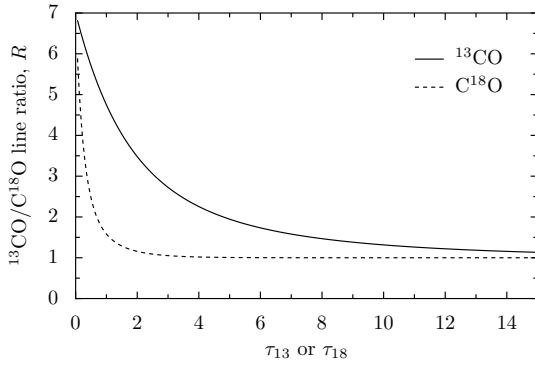
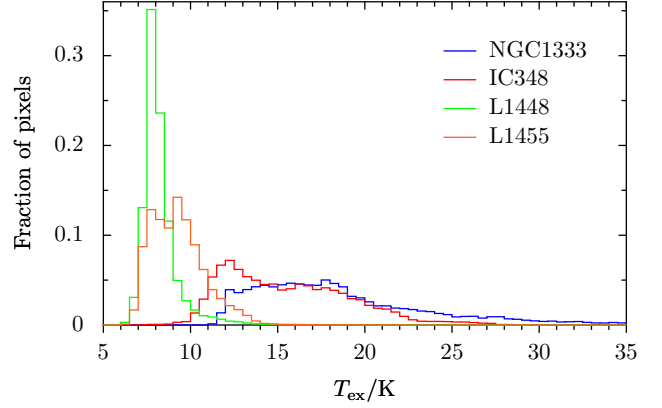


Figure 12. Variation of R with τ for $\zeta = 7$.



Region	$\langle T_{\text{ex}} \rangle$ (K)	σ_T (K)	Median T_{ex} (K)
NGC1333	19.3	7.0	17.7
IC348	15.5	3.6	15.0
L1448	8.2	1.0	8.0
L1455	9.3	1.6	9.2

Figure 14. T_{ex} derived from peak ^{12}CO values. σ_T is the standard deviation of T_{ex} .

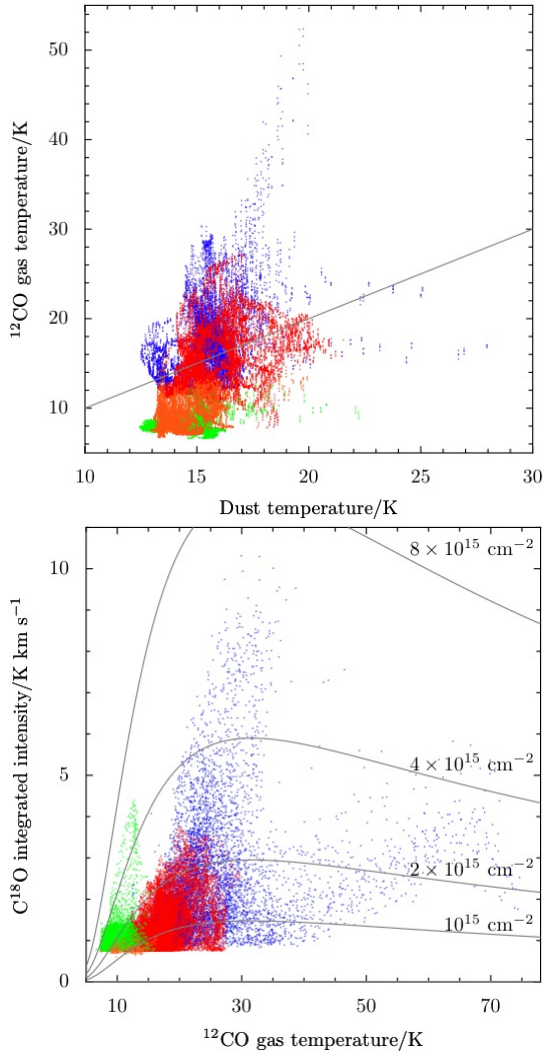


Figure 15. Points mark pixels in the various regions' maps: NGC1333 (blue), IC348 (red), L1448 (green) and L1455 (orange). Top: T_{ex} derived from the peak $^{12}\text{CO } T_{\text{A}}^*$ versus the dust temperature derived from *Spitzer* MIPS data at 70 and 160 μm with 40 arcsec resolution (Schnee et al. 2008). The line marks where both temperatures are equal. Bottom: C¹⁸O integrated intensity versus ^{12}CO derived T_{ex} . The lines denoted the anticipated dependence for constant column densities of C¹⁸O as labelled.